ULSAN NATIONAL INSTITUTE OF
SCIENCE AND TECHNOLOGY

State-dependent alignment effect at dispersion of carbon disulfide molecules by a pulsed optical standing wave

Byung Gwun Jin

Department of Chemistry

Graduate School of UNIST

State-dependent alignment effect at dispersion
of carbon disulfide molecules by a pulsed
optical standing wave

A thesis/dissertation
submitted to the Graduate School of UNIST
in partial fulfillment of the
requirements for the degree of
Master of Science

Byung Gwun Jin

07 / 10 / 2019 of submission

Approved by
_____
Advisor
Bum Suk Zhao

State-dependent alignment effect at dispersion
of carbon disulfide molecules by a pulsed
optical standing wave

Byung Gwun Jin

This certifies that the thesis/dissertation of Byung Gwun Jin is approved.

07 / 10 / 2019 of submission

signature

_____

Advisor: Bum Suk Zhao

signature

_____

Oh Hoon Kwon

signature

_____

Thomas Schultz

Abstract

The optical dipole force using nonresonant optical field has been studied as an important tool to manipulate the center-of-mass motion of molecules. When the non-spherical molecules are in an optical field, the rotational states of the molecules are hybridized and thereby the dipole moment, which is induced in the molecules by the optical field, is aligned or oriented with respect to the polarization direction of the optical field. Because the imparted optical force is proportional not only to the gradient of the interaction potential between the optical field and the field-induced dipole moment but also to the molecular polarizability that depends on the molecular rotational states, the molecular polarizability with the rotational state-dependent alignment must be considered to interpret the optical dipole force.

Here, we demonstrate the dispersion of carbon disulfide molecules using an optical standing wave to show the distinct effect of the state-dependent alignment. The experiments are performed at stagnation pressure of 81 and 21 bar, with rotational temperatures estimated as 1 and 35 K, respectively. The effect of the molecular alignment becomes weak at high rotational temperature because the molecules are distributed in high rotational states. We chose carbon disulfide as a target molecule because the polarizability of the linear molecules along the molecular axis is larger than its perpendicular components when the molecules are aligned within the field so that it can be manipulated effectively. The theoretical simulations of dispersion trajectories are compared using the Monte-Carlo method to verify the state-dependent alignment effect. At the low rotational temperature, the state-dependent effect appears in the molecular dispersion with increasing field intensity. These results verify that the state-dependent alignment is required to interpreting the optical dipole force correctly.

Contents

List of figures

1. Background

1.1 Introduction

The manipulation of small particles using an optical force took the first step with a pioneering work of Ashkin and co-workers in 1970 [1]. In that paper, they achieved the acceleration and trapping of tiny latex spheres using the focused laser beam. Based on their study, they proposed that the optical force is applicable to manipulating the center-of-mass motion of atoms and molecules. Afterward, the optical force has been studied extensively as an important tool to manipulate the atoms and molecules at a wide range of fields. Especially, this subject has attracted great attention from atomic and molecular physics. As atom-optical components, the optical fields are applicated to a lens [2], a diffraction grating [3] and a mirror [4]. Since molecules are much abundant than atoms in nature, the application for molecules has been studied to such as lenses [5-7], prisms [8-10], as well as decelerators [11-15]. One of great research about optical forces is about cooling and trapping methods of atoms and molecules with laser beams, which was a topic of the Nobel prize award for Physics in 1997 [16-18]. Furthermore, the laser cooling technique made it possible to observe Bose-Einstein condensate (BEC) which is predicted by Bose and Einstein in the early 1920s [19,20]. This achievement is recognized by the Nobel Prize for Physics in 2001 [21,22]. Even in the biology field, the optical force is applicated usefully as an optical tweezer to control a single DNA molecule [23,24], proteins [25,26], and biological particles like a bacteria and virus [27-29].

As aforementioned, the understanding optical dipole force to manipulate molecules is of important in various field. The optical dipole force is directly related to the molecular polarizability with considering laser-induced alignment in the nonresonant laser field. Here, the induced alignment is affected from the rotational state of molecules. In order to interpret the optical dipole force correctly, the understanding of polarizability should precede that. However, the molecular polarizability didn't use to be considered significantly. Herein, the dispersion of carbon disulfide molecules is demonstrated using an optical standing wave to show the effect of the state-dependent alignment.

The conceptual schemes for the molecular dispersion are illustrated in Fig. (1). Figure 1(a) shows a case for the absence of an optical field. The molecular beam goes through directly to the detector without any force since there is no extra field. If the optical standing wave lies in the path of the molecular beam as shown in Fig. 1(b), the molecules experience the optical force to the laser-propagating direction and then they are dispersed. The effect of the molecular alignment become weak at high rotational temperature because the molecules are distributed in high rotational states. Thus, we employed two different source pressure to make the different rotational temperature of the molecules. Carbon disulfide, one of the typical linear molecules, is chosen as a target molecule who has a large polarizability

1

component along the molecular axis while perpendicular components are small. This polarizability anisotropy allows the molecules to be manipulated facilely by an optical field. The theoretical simulations of dispersion trajectory are compared using the Monte-Carlo method to verify the state-dependent alignment effect with different rotational temperature. This study will help us to understand and tailor the optical dipole force with the state-dependent alignment effect accurately.
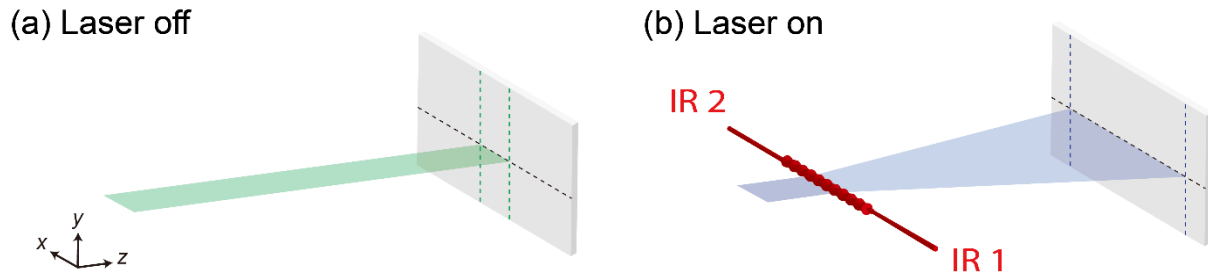

Figure 1. Conceptual schemes for the molecular dispersion. (a) The molecular beam, indicated as a green beam, goes through a field-free space, thereby the initial velocity of the molecular beam doesn't change at all. The molecules are detected at the final position between the green dash lines with maintaining their initial velocity. (b) When a nonresonant optical standing wave is exerted on the molecular beam (blue beam), the molecules who pass through the standing wave can experience the optical dipole force along the laser propagating axis. As a result, the molecules are accelerated along the laser propagating axis. The final position of the dispersed molecules is within the blue dashed lines.

1.2 Manipulation of atoms

The optical dipole forces on atoms can be formed not only by a near-resonant optical field, but also a nonresonant optical field. When an atom is exposed by a resonant laser, a linear momentum $\hbar k$ of a photon can be transferred to the atom. After the absorption of the momentum, the atoms release photons into a random direction. In the photon emitting process, the momenta of the atom are changed as much as $n\hbar k$ along the laser propagating direction with n-cycles of absorptions and emissions. Such reversible energy transfer creates an optical dipole force acting on the atoms. This energy transfer cycle makes it possible to cool and trap atoms [18,30]. Due to the resonance property of the absorption, it doesn't require a strong laser intensity when the frequency of the laser is matched to the target atoms. One of the well-known cooling techniques is Doppler cooling which employs a red-detuned laser. Here, the atoms can absorb the red-detuned light only when the detuned laser becomes resonant with atoms that move toward the laser beam while the laser is off-resonant with the rest of the atoms. Therefore, the cooling of atoms is achieved because fast atoms lose their kinetic energy.

The optical dipole force can be exerted on atoms with a nonresonant optical field based on the

polarizability of atoms [31]. It implies that this technique can be applied as a general method to control atoms and molecules. However, the interaction between the atoms and the nonresonant laser field is so weak that it is hard to obtain a sufficient optical force using a continuous laser beam. Thereby, it requires a pulsed laser with a strong laser intensity to achieve a measurable optical dipole force on the atoms. On the other hand, the strong nonresonant field can exert a strong optical dipole force to any atoms without cooling them. It is especially useful to manipulate inert atoms such as helium or argon. For example, the focusing of neutral xenon gas is reported by Barker and co-workers using an IR pulsed laser which forms a far-off resonant optical field with a xenon atom [32].

1.3 Manipulation of molecules

Applying the optical dipole force to molecules is more complicated than the atomic case and it is difficult to employ a resonant optical field because of their complex energy structure. The molecules can fall into dark states easily, which cannot absorb and emit photons, during the energy transition. Thus, it is difficult to maintain the energy transition cycles required for control of molecules with a resonant laser. Only few achievements of decelerating and cooling are reported using simple and specific molecules, mostly diatomic molecules. One of the reported molecules is strontium monofluoride (SrF). Researchers achieved a cooling of the molecules down to a few millikelvin using the magnetic field of a Helmholtz coil [33,34] and a quadrupole [35], which together are called the magneto-optical trap (MOT) [33-35]. In this research, they employed repumping lasers to prevent the molecules from falling into dark states. The deceleration of yttrium monoxide (YO) is also reported recently [36]. In that case, microwaves are mixed with resonance optical fields. Because of the difficulties of the molecular manipulation using resonant optical field, the nonresonant optical dipole force has been studied extensively as a general tool for molecular manipulation.

When a molecule is in a nonresonant optical field, a dipole moment is induced in the molecule. The interaction between the electric field of the laser and the dipole leads to the optical Stark interaction, and consequently, the Stark interaction creates an optical dipole force acting on the molecules. It requires an intense laser field because the induced dipole is too weak to get enough force to manipulate the molecules under the continuous beam laser. Therefore, the pulsed lasers are employed usually to create an optical dipole force. The Stark interaction potential U between a molecule in the ground state and a laser intensity I can be described as below [37, 38]:

$$U = -\frac{1}{4}\alpha E^2 = -\frac{1}{2}Z_0\alpha I, \tag{1}$$

where α is the polarizability of the molecule and E is the electric field of the laser, and Z_0 is vacuum

impedance. This relationship tells us that the ground state molecules in the nonresonant optical field are always high field seekers because the eigenvalues of the ground state are shifted to lower energy as the field intensity increases [39]. It means that the molecules are forced toward the center of an inhomogeneously distributed optical field such as a molecular lens when the optical field is formed by a TEM$_{00}$ Gaussian beam. Here, the spatial gradient of the interaction potential is the attractive optical force $\mathbf{F} = -\nabla U$ on the molecules. Thus, the optical dipole force can be enhanced by making the field gradient steeper.

The optical dipole force has been used to create molecule-optical components like a lens or a prism. Deflection and focus of neutral molecules are demonstrated with carbon disulfide [5-7, 10], benzene [7,8] and nitric oxide [8], via a focused nonresonant pulsed laser beam. The molecules are deflected when they pass near the center of the focused laser beam. Here, the applied force is proportional to the polarizability of the molecule. Hence, the molecular separation is proposed based on different molecular polarizabilities. In the research, benzene is deflected more than nitric oxide because the polarizability-to-mass ratio of benzene is larger than the ratio of nitric oxide [8]. Not only the re-direction of molecules but also acceleration and deceleration have been studied using a single focused laser beam. When the focused laser beam and the molecular beam are orthogonal to each other, the molecules that pass through the center of the focused laser beam experience a force along their propagating direction. This was suggested theoretically [40] and demonstrated using benzene [11] and carbon disulfide molecules [12]. As an extension of the study, the slowing of molecules has been studied via an optical lattice potential. Deceleration of hydrogen molecules was obtained by crossing two identical laser beams that consist of two counter-propagating laser beams at a shallow angle [13]. Here, the optical dipole force can be enhanced by an optical standing wave because a potential gradient induced by the optical standing wave is steeper, even the depths of their potential are same.

Furthermore, it has been tried to achieve the rapid deceleration of the target molecules by a constantly moving interaction potential. In the standing wave potential, the molecules that undergo a half rotation in the phase space are decelerated most. It was demonstrated by slowing nitric oxide [14] and benzene [15]. In those studies, a moving optical lattice is formed by the intersection of near-counter-propagating laser beams. Here, one of the two laser beams is chirped to control the time-dependent frequency, so that the optical lattice becomes moving in the reverse direction of the molecular beam. As a result, they showed the slowing of molecules and proposed a general and effective way to control the molecular longitudinal motion by a moving standing wave.

On the other hand, selection of molecules in particular rotational states has been studied using an optical standing wave, which is formed by two identical counter-propagating laser beams [9, 41]. In that study, the optical standing wave leads to the transverse acceleration of neutral carbon disulfide molecules. As it was mentioned previously, the alignment effect, which is related to the molecular

rotational state, should be considered to interpret the optical dipole force. Thus, a sufficiently low rotational temperature is desirable to create a clear state-dependent alignment effect because the effect of the rotational states might be smeared out when the molecules occupy rotational states of large rotational energy with a wide distribution at high rotational temperature. The previous dispersion experiments were performed with a rotational temperature of 35 K [9]. However, the alignment effect wasn't considered. Afterward, the theoretical study of molecular dispersion was carried out with considering rotational state-dependent alignment effect at a rotational temperature of 1K and 35 K to show the distinct effect of rotational state-dependent alignment [41]. However, this wasn't demonstrated experimentally, yet. Thus, this thesis is written to demonstrate the rotational state-dependent alignment effect.

1.4 Adiabatic alignment and orientation of molecules

Alignment or orientation effects of molecules are of interest for the interpretation of various physical phenomena involving molecules because most molecules are anisotropic. Here, the term of alignment (orientation) describes a state where the molecular axes are parallel to each other without (with) considering their head and tail direction. The control of alignment and orientation of molecules has been regarded as an essential technique to understand steric dynamics. Until a few decades ago, molecular alignment (or orientation) was poorly studied. A molecule whose permanent dipole moment is extremely large can be oriented by a strong electrostatic field, named brute force alignment [42]. On the other hand, the orientation of polar molecules (CH_3Cl and CHF_3) was tried by using inhomogeneous electrostatic fields formed by a hexapole in 1990 [43]. All of the aforementioned studies were for the polar molecules that have a permanent dipole moment. However, it is hard to apply this to nonpolar molecules that don't have a permanent dipole moment. Thereby, lots of research has been tried to align nonpolar molecules. The aligning method of nonpolar molecules is based on the induced dipole under the strong nonresonant laser field [37,44]. In the interaction potential, the molecules show the limited angular motion, which is called pendular motion, with the eigenstates consisting of hybridization of its field-free rotational state, namely pendular states. Here, the rotational states with the quantum numbers J and M, where J and M describe quantum numbers associated with the molecular angular momentum and its projection onto the laser polarization axis, respectively, are transitioned adiabatically to specific pendular states by an intense laser field. This process occurs slowly relative to the molecular rotation period, which is called the adiabatic process [45]. Thus, the adiabatic process requires a longer laser pulse duration than the molecular rotational period. When the molecules occupy low-lying rotational states, the transition to well-aligned pendular states, which are in lower energy states, is preferred. Consequently, the degree of molecular alignment can be increased by lowering the rotational temperature of molecules. The alignment experiments were performed with various nonpolar molecules

such as I_2 [46], ICl, CS_2, CH_3I and C_6H_5I molecules [47] using a pulsed single longitudinal mode laser. As the technique developed, the orientation techniques have been developed further by combining electrostatic field with an intense nonresonant laser field. This concept was designed in 1999 [48,49] and then the first experiment was performed for a polar molecule of OCS using a linearly polarized laser pulse and electrostatic field [50]. Since the OCS molecule is a linear molecule, the molecular axis is oriented along the laser polarization axis of the laser field, which is termed one-dimensional orientation. Afterwards, the molecular alignment and orientation was demonstrated in one- and three-dimension using larger molecules such as iodobenzene [51], 3,4-dibromothiophene [52] and 2,6-difluoroiodobenzene [53]. For the three-dimensional alignment and orientation, an elliptically polarized laser beam was used. Under the elliptically polarized laser beam, the largest polarization axis and the second most polarizable axis of a molecule can be aligned along the major axis and minor axis of the elliptical optical field, respectively. Therefore, the molecule in the elliptically polarized optical field can be aligned in three-dimension.

2. Theoretical development

2.1. Interaction potential and optical dipole force

The interaction potential between a $^1\Sigma$ molecule, such as a linear molecule CS_2 in the ground state, and a laser field with the intensity I can be described as below:

$$U_{J,M} = -\frac{1}{2}\left(\alpha_\parallel \cos^2\theta + \alpha_\perp \sin^2\theta\right)Z_0 I$$

$$= -\frac{1}{2}\left[\left(\alpha_\parallel - \alpha_\perp\right)\cos^2\theta + \alpha_\perp\right]Z_0 I, \tag{2}$$

where $\alpha_\parallel$ and $\alpha_\perp$ are the polarizability components which are parallel and perpendicular to the molecular axis, respectively. The polar angle θ means an angle between the molecular axis and the polarization axis of the laser field. The symbol of the vacuum impedance is Z_0. Here, the intensity I of the standing wave is given by

$$I = 4I_0 \exp\left[-\frac{2(y^2+z^2)}{\omega_0^2}\right]\exp\left[-4\ln(2)\frac{t^2}{\tau^2}\right]\cos^2\left(\frac{2\pi}{\lambda}x\right), \tag{3}$$

where I_0, ω_0, τ and λ are the peak intensity, waist radius, pulse duration as a full width at half maximum (FWHM) and wavelength of the laser beam, respectively. Herein, we use a nonresonant laser with the wavelength of 1,064 nm. The waist radius was estimated as 21.5 μm with the pulse duration of 7.5 ns.

When the laser field isn't exerted ($I = 0$), all molecules rotate freely. It is represented by the Hamiltonian $\mathbf{H}_0 = B\mathbf{J}^2$, where $\mathbf{J}^2$ is the square of angular momentum operator and B is a rotational constant of the molecule. For CS_2 molecule, the rotational constant is 0.109 cm^{-1}. The rotational motion of the molecules can be described by the spherical harmonics $Y_{j,M} = |j,M\rangle$, where j is the rotational angular momentum quantum number and M is the projection of the angular momentum on the laser polarization axis. In the case of $^{12}C^{32}S_2$, quantum number j can be even integers only because ^{32}S has the zero nuclear spin [54].

When the molecules are in the interaction field ($I > 0$), the angular motion of the molecules is limited, like a pendulum. Here, the eigenstates of the molecule, namely pendula states, consist of the superposition of the field-free rotation, $\Psi_{J,M}(I) = \sum_J C_j^{J,M}(I)|jM\rangle$ for a linear molecules [55]. The

rotational states with the quantum states *J* and *M* are transitioned adiabatically to specific pendular states by a strong laser field. Consequently, the molecular axes are aligned about the polarization vector of the laser field. The adiabatic process occurs slowly relative to the period of the molecular rotation. Thus, the adiabatic alignment requires a longer laser pulse duration than the molecular rotational period. In our system, the laser pulse duration (7.5 ns) is much larger than the rotational period of CS_2 molecules (49 ps), so it undergoes alignment adiabatically. If the molecules occupy low-lying rotational states, the transition to well-aligned pendular states which are in lower energy states is preferred. Consequently, the degree of molecular alignment can be increased by decreasing the molecular rotational temperature. For the adiabatic alignment process, the wave function of aligned molecules can be described by the time-independent Schrödinger equation with the perturbed Hamiltonian $\mathbf{H} = \mathbf{H}_0 + U$, thus $\mathbf{H} = B\mathbf{J}^2 + U$. Within the laser field, the degree of molecular alignment can be represented by the expectation value of $\cos^2\theta$, which is termed alignment cosine. The expectation value of the alignment cosine $<\cos^2\theta>_{J,M}(I)$ with rotational states *J* and *M* can be obtained by $\left\langle \Psi_{J,M}(I) \left| \cos^2\theta \right| \Psi_{J,M}(I) \right\rangle$. It shows the degree of

alignment of molecules is relied not only to the intensity of the laser field but also their rotational states. In this paper, we write $<\cos^2\theta>_{J,M}$ as the same meaning as $<\cos^2\theta>_{J,M}(I)$ for convenience. We can describe the interaction potential with considering rotational state-dependent alignment effect of the molecules as below:

$$U_{J,M}(\mathbf{r},t) = -\frac{1}{2}\left[\left(\alpha_\parallel - \alpha_\perp\right)\left\langle\cos^2\theta\right\rangle_{J,M} + \alpha_\perp\right]I(\mathbf{r},t)Z_0$$

$$= -\frac{1}{2}\alpha_{J,M}^U[I(\mathbf{r},t)]I(\mathbf{r},t)Z_0. \tag{4}$$

Here, we reformed the equation for interaction potential with the effective polarizability

$$\alpha_{J,M}^U = \left(\alpha_\parallel - \alpha_\perp\right)\left\langle\cos^2\theta\right\rangle_{J,M} + \alpha_\perp, \tag{5}$$

including the molecular rotational state-dependent alignment along the laser polarization axis [56].

Since the optical dipole force F due to the interaction field is the gradient of the potential, it can be written as

$$\mathbf{F} = -\nabla U_{J,M}(\mathbf{r},t)$$

$$= \frac{1}{2}Z_0\nabla\left\{\alpha_{J,M}^U[I(\mathbf{r},t)]I(\mathbf{r},t)\right\}$$

8

$$= \frac{1}{2} Z_0 \nabla I(\mathbf{r},t) \left\{ \alpha_{J,M}^U [I(\mathbf{r},t)] + I(\mathbf{r},t) \frac{d\, \alpha_{J,M}^U [I(\mathbf{r},t)]}{d\, I(\mathbf{r},t)} \right\}. \tag{6}$$

Here, the polarizability $\alpha_{J,M}^U (I)$ is substituted as $\alpha_{J,M}^F (I)$ with its gradient term to describe the force directly.

$$\alpha_{J,M}^F (I) = \alpha_{J,M}^U (I) + I(\mathbf{r},t) \frac{d\, \alpha_{J,M}^U [I(\mathbf{r},t)]}{d\, I(\mathbf{r},t)}. \tag{7}$$

Thus, the exerted force can be rewritten simply as below:

$$\mathbf{F} = \frac{1}{2} \alpha_{J,M}^F (I) Z_0 \nabla I(\mathbf{r},t). \tag{8}$$

The equation shows clearly that the optical force $\mathbf{F}$ is directly proportional to both the polarizability and gradient of the interaction potential. These effective polarizabilities $\alpha_{J,M}^U (I)$ and $\alpha_{J,M}^F (I)$ facilitate interpretation of the interaction potential U and the optical dipole force $\mathbf{F}$ due to the interaction field.

2.2. Effective polarizability

As we discussed previously, we need to consider the effective polarizability $\alpha_{J,M}^U (I)$ and $\alpha_{J,M}^F (I)$ involving the rotational states-dependent alignment of the molecules with the laser field intensity I for the interaction potential and the optical dipole force, respectively. Figure 2 shows the effective polarizabilities for CS_2 molecules with the quantum number J and M against laser intensity I as three rows. From the top to bottom, each row corresponds to the condition of $J \leq 4$, $J = 10$, and $J = 20$, respectively. For the same J value, the polarizability lines for various $|M|$ value are represented by different brightness; the higher $|M|$ value, the darker lines. Here, the calculation of the effective polarizability is focused on the rotational temperature T_{rot} of 1 and 35 K because the rotational temperatures of the experiments are estimated as 1 and 35 K. For $T_{\text{rot}} = 1$ K, the population of the rotational states is the largest at $J = 2$ and the near-half maximum at $J = 0$ and 4. At $T_{\text{rot}} = 35$ K, the population of the rotational states has its maximum at $J = 10$ and near-half of the maximum at $J = 2$ and 20. In the second row of Fig. 2, the black and red solid lines indicate the state-averaged polarizabilities with considering rotational state distribution for $T_{\text{rot}} = 1$ and 35 K, respectively. Here, the effective

polarizability curves show different aspect from the averaged polarizabilities curves definitely. Furthermore, we can confirm that the effective polarizability is larger generally at 1 K than at 35 K until they converge to the high-field limit:

$$\alpha_{J,M}^{U}(I) = (\alpha_{\parallel} - \alpha_{\perp})\left(1 - \frac{J_i + 1}{\sqrt{(\alpha_{\parallel} - \alpha_{\perp})Z_0\pi/2B}}I^{-1/2}\right) + \alpha_{\perp}, \tag{9}$$

for $(J - |M|)$ is even number and

$$\alpha_{J,M}^{U}(I) = (\alpha_{\parallel} - \alpha_{\perp})\left(1 - \frac{J_i}{\sqrt{(\alpha_{\parallel} - \alpha_{\perp})Z_0\pi/2B}}I^{-1/2}\right) + \alpha_{\perp}, \tag{10}$$

for $(J - |M|)$ is even number [37,44]. In the Fig.2, the polarizabilities for even $(J - |M|)$ are drawn as solid lines while the curves of odd $(J - |M|)$ are drawn as dashed lines. To make the molecules reach the high-field limit, the larger rotational energy molecules have, the stronger laser intensity is required. If the molecules are, however, close to the high-field limit by intense laser field, the state-dependent alignment effect in molecular dispersion becomes diluted because each polarizability is converged closely. Thereby, the molecular dispersion should be demonstrated relatively weak intensity, such as 10×10^{10} W/cm^2, to obtain the various dispersion aspect of each polarizability.

In the standing wave field, the field intensity is a function of time and space. Thus, the effective polarizability $\alpha_{J,M}^{U}(I)$ and the interaction potential U can be expressed for the intensity variation of the given standing wave. Figure 3(a) shows the spatial intensity variation of a pulsed standing wave field along the x-axis at the center of space ($y = z = 0$) and time ($t = 0$). When the standing wave consists of two laser beams with the peak intensity $I_0 = 3.2 \times 10^{10}$ W/cm^2, the maximum intensity of the standing wave becomes $4I_0 = 13 \times 10^{10}$ W/cm^2. Figure 3(b) shows the alignment cosine $\langle\cos^2\theta\rangle_{J,M}(I)$ (left scale) with the corresponding molecular polarizability $\alpha_{J,M}^{U}(I)$ (right scale) at the given laser intensity profile. In Fig. 3(b), the black line is for the rotational states $J = 0$ while the red, blue and green lines correspond to $J = 2$ with $|M| = 0$, 1 and 2. Respectively. Here, $J = 2$ is the most populated rotational state (about 58%) of CS$_2$ molecules at $T_{\text{rot}} = 1$ K. Generally, $\alpha_{J,M}^{U}(4I_0)$ is larger than $\alpha_{J,M}^{U}(0)$ except for the rotational state of $J = 2$ and $M = 0$ near the standing wave node ($x = \pm0.25\lambda$) with very small I_0. This state contributes minor effect to the optical force since it occupies a small portion compared to all states. Consequently, the interaction potentials $U_{J,M}[I(x)]$ between the molecules and standing wave field are

shown at Fig. 3(c) for each rotational state. Here, the solid lines indicate the potential with considering the alignment effect while the dashed lines correspond the potential without considering the alignment effect. They share the color code with the alignment cosine and its potential curves in Fig. 3(b). Here the red solid curve is hard to distinguish because it is overlapped almost with the green curve.
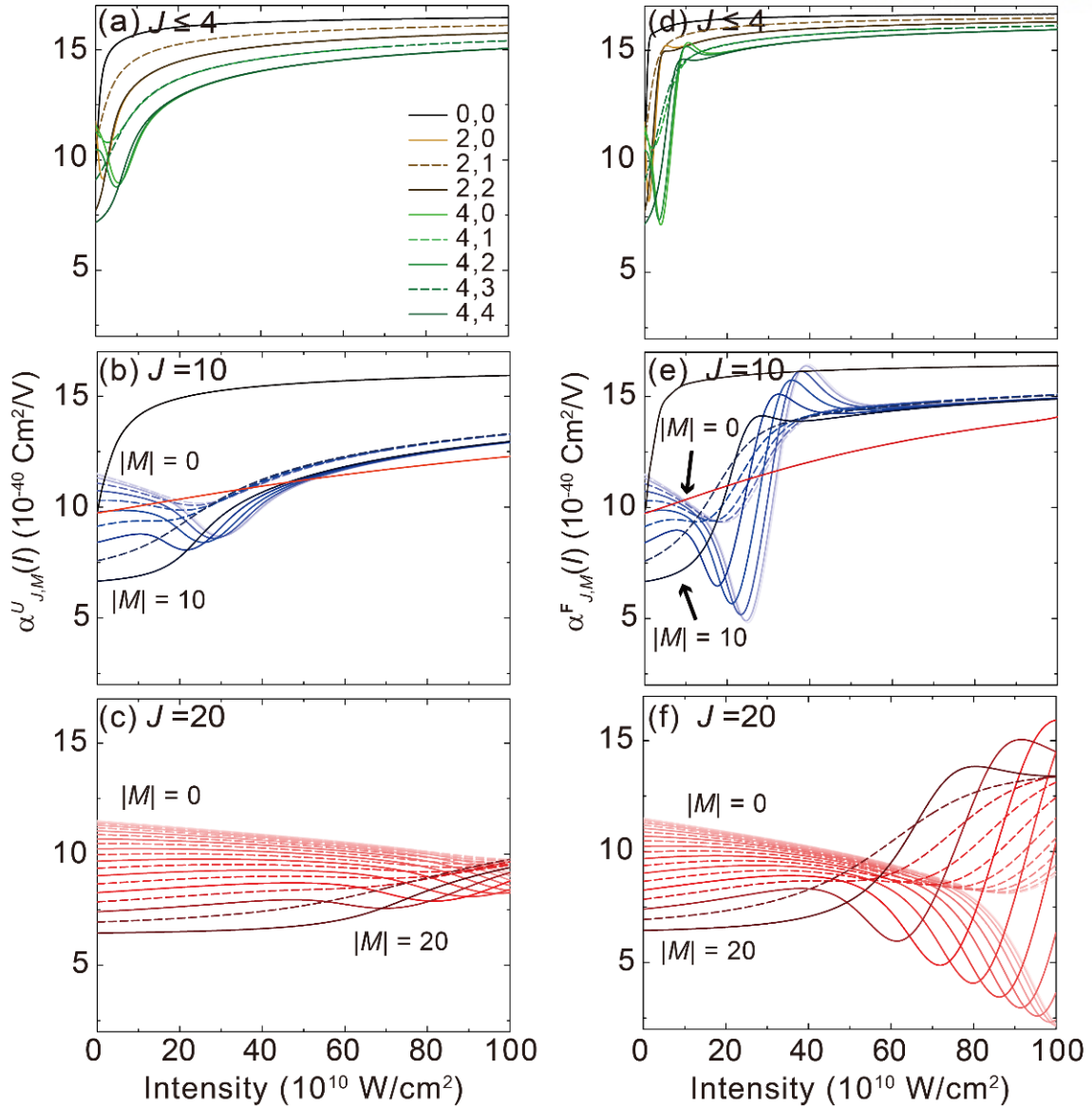
Figure 2. Effective polarizability $\alpha_{J,M}^{U}(I)$ and $\alpha_{J,M}^{\mathbf{F}}(I)$ of carbon disulfide molecules for each rotational state. The effective polarizabilities are plotted as a function of laser peak intensity. From the top to bottom, each row corresponds to the condition of $J \leq 4$, $J = 10$, and $J = 20$, respectively. The polarizability lines of the higher $|M|$ are represented darker lines for same J value. The polarizability for the even and odd $\left(J - |M|\right)$ are drawn as solid and dashed lines, respectively. The state-averaged polarizabilities are plotted using black and red solid lines for $T_{\text{rot}} = 1$ and 35 K, respectively. The aspects of the effective polarizability and state-averaged polarizability are different obviously.
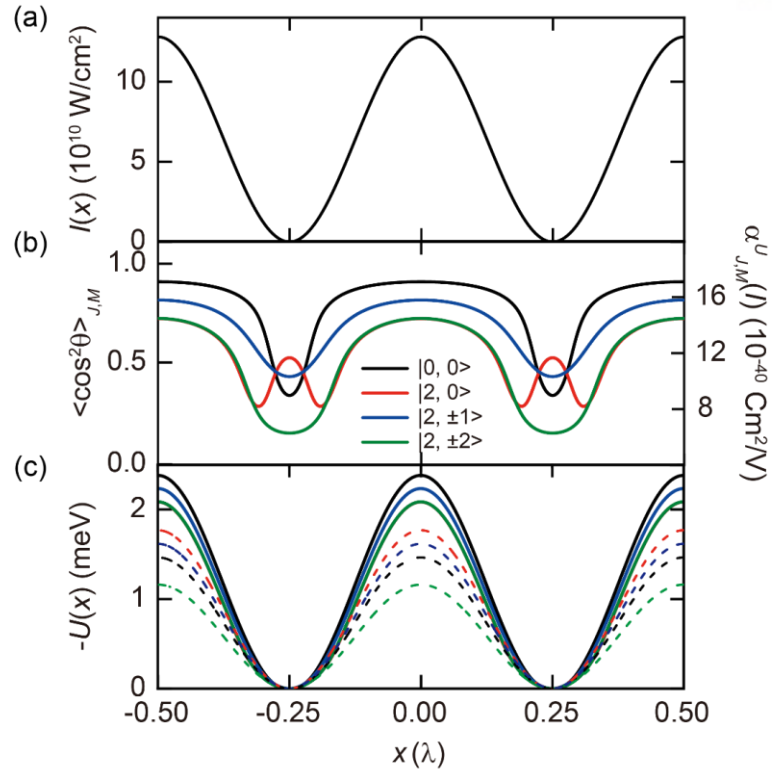
Figure 3. Effective polarizability and corresponding interaction potential along with the given standing wave intensity variation. (a) The intensity profile of an optical standing wave. The profile is calculated along the x-axis at the center of the y- and z-axis ($x = y = 0$) and time ($t = 0$). (b) The alignment cosine (left scale) with the effective polarizability (right scale) considering molecular state-dependent alignment effect at given standing wave field intensity. For the rotational state $J = 0$, the curve is plotted as a black solid line. For the rotational states $J = 2$, the curves have the red, blue and green color for $|M| = 0$, 1 and 2, respectively. (c) The interaction potential of molecules with (solid lines) and without (dashed lines) considering the alignment effect.

3. Experimental

3.1. Experimental setup

The experimental scheme is shown in Fig. 4. Here, every experimental device is synchronized at 10 Hz repetition rate by four digital delay generators. The optical standing wave is formed by two identical counter-propagating IR pulses, namely IR1 and IR2. These IR1 and IR2 are defined to be forward- and backward-propagating beams along the x-axis, respectively. A single IR pulse from an injection-seeded Nd: YAG laser is separated by a beam splitter into IR1 and IR2 pulses to make the counter-propagating IR pulses. Each split IR pulse is adjusted to have equal pulse energy and the same linear polarization direction via two sets of a zero-order half-wave plate and a Glan-laser calcite polarizer. The polarization direction of the IR beams is adjusted to be vertical to the optical table and this direction is chosen as the y-axis in our experimental system. Thus, the z-axis is defined to be orthogonal to both x- and y-axis. The split IR pulses, having identical properties with $\lambda = 1{,}064$ nm wavelength and $\tau = 7.5$ ns FWHM pulse width, propagate the same distance to the detection chamber. At both sides of the detection chamber, along the x-axis, two identical plano-convex lenses with a nominal focal length of 177 mm make each laser pulse focused on the center of the detection chamber. Here, the waist radii w_0 of both focused IR laser pulses are estimated as 21.5 μm.

A pulsed tunable dye laser, which is pumped by a third-harmonic beam from another Nd: YAG laser, is used to tune the wavelength of the probe beam. The wavelength of the probe pulse is tuned to 477.7 nm using Coumarin 480 (Coumarin 102) dye because CS_2 molecules can be ionized through a (3+1) resonance-enhanced multiphoton ionization (REMPI) process with the transition $\left[\frac{1}{2}\right] np\sigma_u \left({}^1\Pi_u\right) \leftarrow \tilde{X} \; {}^1\Sigma_g^+$ [57,58]. In the same way as adjusting IR pulses, the probe pulse is adjusted to have pulse energy of ~1 mJ and linear polarization along the y-axis by a combination of a zero-order half-wave plate and a Glan-laser calcite polarizer. The wavelength difference between IR and probe beams induces a displacement of their foci, namely chromatic aberration. To correct the chromatic aberration, the beam divergences of both the IR and the probe beam are adjusted by combinations of a plano-concave lens and a plano-convex so that the foci of all laser beams are on the same point.

After the adjustment of beam divergence, the probe beam goes through an optical low-pass filter to propagate nearly the same pathway with the IR2 pulse. Then it is focused by the same plano-convex lens focusing the IR2 pulse. The focused probe pulse is separated in time and space along the z-axis from the IR standing wave pulse to avoid multi-color processes and to ionize the dispersed molecules selectively.

A CS_2 molecular beam is generated by an Even-Lavie pulsed valve and directed into a high vacuum chamber with He carrier gas at a stagnation pressure of $P_0 = 81$ and 21 bar. The molecular beam source

is produced by vaporizing CS_2 molecules at a vapor pressure of 427 mbar at 295 K. Under high stagnation pressure, the molecular beam is cooled adiabatically by a supersonic expansion to make the distribution of rotational states narrow, including only low-energy states. At the previous study, the rotational temperature of the molecules was estimated as 1 and 35 K at $P_0 = 81$ and 21 bar, respectively [10]. The rotationally cold molecular beam propagates almost parallel to the z-axis with the most probable initial velocity v_{0z} of 1,740 (1,720) m/s for 81 (21) bar. The pulsed molecular beam is collimated by two skimmers, namely skimmer1 and skimmer2, of 3- and 1-mm diameter. Each skimmer is mounted 170 and 525 mm away from the pulsed molecular valve. After the skimmer2, the molecular beam enters a detection chamber section. At 177 mm downstream of skimmer2, a vertical slit, which has a 200-μm width, makes molecular beam collimated further along the x-axis. Based on the line-of-sight argument, the initial velocity distribution of the molecular beam is determined approximately as the FWHMs $\Delta v_{0x} = 4.3$ and $\Delta v_{0y} = 3.6$ m/s. In the detection chamber, the collimated molecular beam passes through an optical standing wave at a near-perpendicular angle on the x-z plane with very small degrees. By this optical standing wave, the molecular beam is dispersed. After a 30 ns time delay, the tightly focused probe pulse is injected with a distance of 52 μm on the z-axis, which corresponds to the flying distance of the molecules during the 30 ns delay, to ionize the dispersed CS_2 molecules that pass through the vertical center of the pulsed standing wave.

The velocity distribution of CS_2 molecules in the x-y plane is analyzed by the velocity mapping technique [59,60]. For the velocity mapping, an ion lens is set in the detection chamber. The ion lens makes the ionized molecules accelerated and focused onto a microchannel plate (MCP) after flying through a time-of-flight (TOF) tube of 342-mm length. Here, the ions who have the same initial velocity are mapped onto the same position onto the MCP. This ion lens consisted of three electrodes made from a thin stainless steel plate, which are a repeller, an extractor and a ground, whose thickness and diameter are 2 mm and 90 mm, respectively. The electrodes are coaxial with the z-axis and spaced 16 mm apart along the z-axis. While the repeller has a hole of 4-mm diameter at the center, the extractor and the ground have a 20-mm diameter hole at the center of them. To fulfill the velocity map imaging condition, the repeller and the extractor are charged as 900 and 644 V, respectively.

The ion signals are amplified and converted into luminescence signal by a set of a Chevron-type MCP and a phosphor screen(P47). After the conversion to luminescence signals, an intensified charged-coupled device (ICCD) camera captures the image of ions. On the other hand, a photomultiplier tube (PMT) also detects the luminescence signal and transfers it to a digital oscilloscope. Using the signal from the PMT, we monitor the TOF spectrum to gate the imaging devices. Therefore, these imaging devices can be regulated to record CS_2^+ ion signals only.
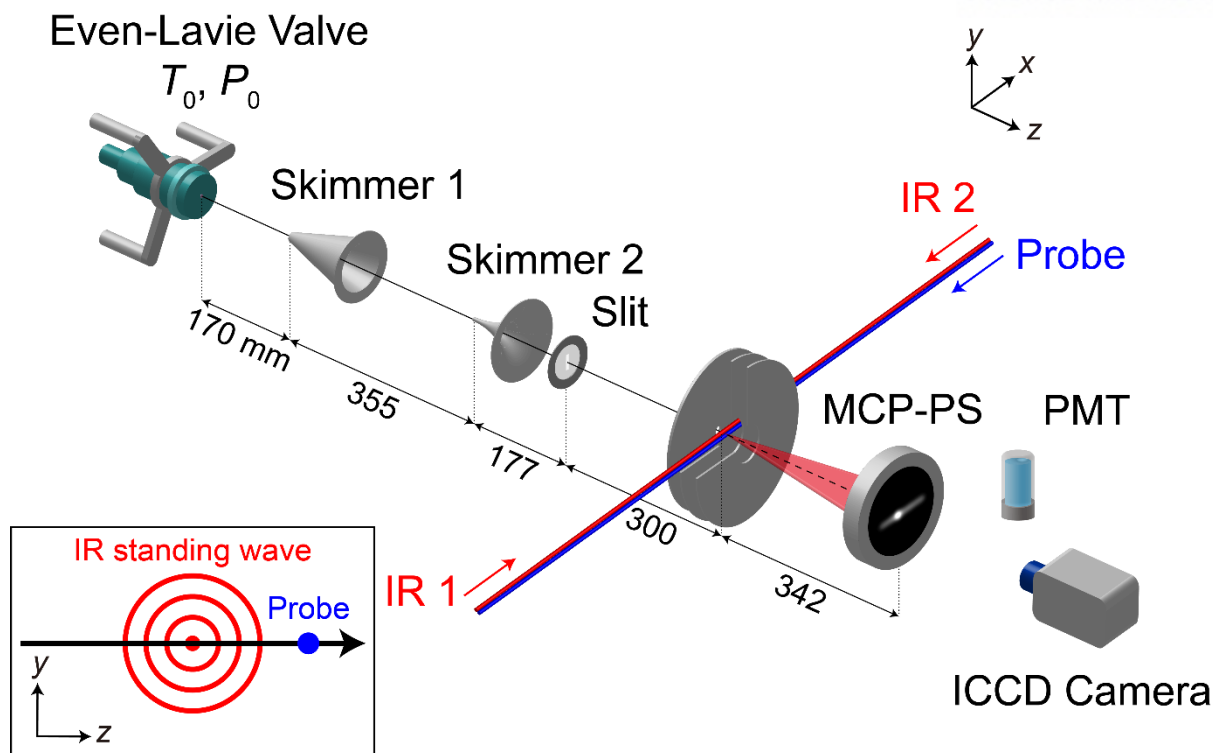
Figure 4. The experimental setup for the experiment. The CS_2 molecular beam is generated by the Even-Lavie pulsed valve with the source pressure of 81 and 21 bar. The propagating molecular pulse is collimated by set of two skimmers and a slit. This collimated molecular beam is dispersed by the optical standing wave, which is created by two counter-propagating IR beams along the *x*-axis. After a delay of 30 ns and adjusted spatial separation from the IR beam, the molecules are ionized by REMPI process with a probe laser. The molecular ions are detected by the combination of microchannel plate (MCP) and phosphor screen (PS). The ions are mapped onto the detector plan with their velocity regardless of their initial positions, namely velocity-mapping. For the velocity-mapping system, the voltages of 900 and 644 V are applied to the repeller and the extractor electrodes. The detected 2-dimensional ion images are obtained by an ICCD camera. The ion signal from the phosphor screen is detected simultaneously to monitor the time-of-flight signal.
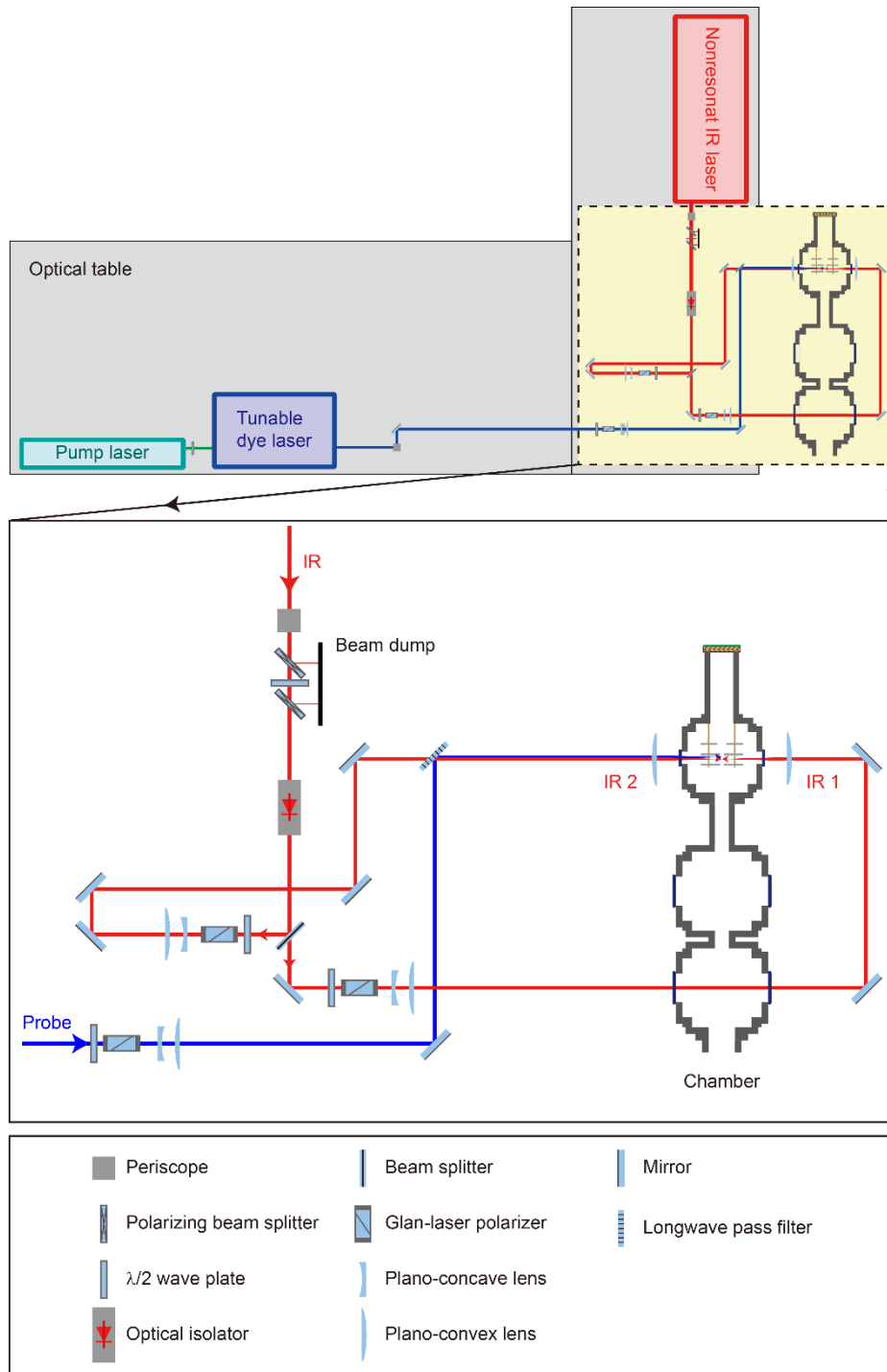
3.2. Optical layout

Figure 5. The optical layout for the experiment. The optical components with the laser lines are shown here. For the detail of optical layout, the main section (yellow shaded region) is magnified above with labels for each optical component. The nonresonant IR beam and the probe beam is indicated using red and blue lines, respectively. The IR beam is split by a beam splitter. These split two IR beam are adjusted to have same intensity and laser polarization axis.

The layout of the optical system is shown in Fig. 5. The main section of optical components is indicated in a black dashed yellow rectangular box. For the details of the optical layout, a magnified scheme of the main section is represented with labels of the optical components. The IR laser beam (red solid line) is filtered by two polarizing beam splitters with 10000:1 extinction ratio and a zero-order half-wave plate to extinct other polarization components. Here, the half-wave plate is located between two polarizing beam splitters to control the laser pulse energy primarily. Then, the IR beam passes through a Faraday optical isolator to prevent damage on the laser instruments from a counter-propagating laser beam. After that, a non-polarizing plate beam splitter divides the IR beam into IR1 and IR2 beam identically. The pulse energies of the split IR beams are modulated by two sets of zero-order half-wave plate and a Glan-laser calcite polarizer to make laser intensity equal. The combinations of a plano-concave lens and a plano-convex lens whose nominal focal length f are 150 and 200 mm, r espectively, are used to adjust beam divergence of the split IR beams. After the split IR beams propagate same distant to the vacuum chamber, each beam is focused by the 177-mm-focal-length plano-convex lenses. The laser intensity and divergence of the probe beam are adjusted as the IR beam is. Here, the combinations of a plano-concave lens and a plano-convex lens have a nominal focal length of 150 and 250 mm, respectively.

4. Result and discussion

4.1 Simulated dispersion of the molecules

As a sampling method, the Monte Carlo method is applied for the simulation with the initial velocities (v_{0x}, v_{0y}, v_{0z}) and initial positions (x_0, y_0, z_0) of each individual molecule, whose distributions are given by a Gaussian function. The molecular initial position on the z-axis z_0 is determined by an equation of $z_0 = v_{mp,z}t_{det} - v_{0z}t_{simul}$, where the most probable velocity $v_{mp,z}$ of 1,740 m/s with FWHM of 174 m/s. In the equation, t_{det} and t_{simul} are the detection time and total simulation time, respectively. Thus, the individual molecule arrives at the detection plane $z = v_{mp}t_{det}$ at $t = t_{det}$. Here the pulse duration of 4 ns and waist radius of 5 μm for the probe beam are included to the detection time and position. In our simulation, we set $t = 0$ when the molecules are pass through the center of the IR laser beam, which has 1 ns jitter. The molecules who passed the IR laser beam are ionized after 30 ns by the probe beam, thereby the detection time $t_{det} = 30$ ns in our time frame with the total simulation time of 60 ns. For the transverse axis, x_0 and y_0, the position of molecules is chosen randomly within a 200-μm-long line and a Gaussian distribution with a 2.9-μm wide FWHM, respectively.

Since the optical force exerted on a molecule is defined as $\mathbf{F}_{J,M}(x,y,z,t) = -\nabla U_{J,M}(x,y,z,t)$, the velocity change of molecules passing through a standing wave is calculated by the following equation:

$$\Delta v_i = \int \frac{1}{m} F_i(x,y,z,t)\,dt \quad (i = x, y, z), \tag{11}$$

where m is a molecular mass. By calculation using 20,000 molecular trajectories for the changed velocity $v_i = v_{0i} + \delta v_i$ ($i = x, y, z$), we obtain the transverse velocity distribution function. If the standing wave field is absent, there is no optical force. Therefore, the final velocity distribution is equal to the initial transverse velocity distribution when the field intensity is zero.

For the precise simulation, we need to understand that the resulting velocity functions are convoluted functions, mainly of the velocity distribution of the initial transverse velocity, velocity change electron recoil during ionization, and detector blurring. We approximate the initial transverse velocity distribution of the molecule beam as a two-dimensional Gaussian function centered at initial velocity of $<v_{0x}> = 10$ m/s and $<v_{0y}> = 0$ m/s with FWHMs of $\Delta v_{0x} = 4.3$ and $\Delta v_{0y} = 3.6$ m/s. Here, we estimated $<v_{0x}> = 10$ m/s by fitting with the obtained data. The velocity change by electron recoil is estimated as 2.7 m/s in the given REMPI process [12]. The FWHMs of the detector blurring is estimated to 12.9 ± 1.5 and 13.3 ± 1.5 m/s for x- and y-axis, respectively, by analyzing profiles of single ion images. Since the detector blurring is dominant in our experimental system, the velocity distribution in the absence of

the laser field is dominated by the detector blurring.

4.2 Experimental result

The velocity map images of CS_2 molecules are measured of various condition: the stagnation pressure P_0 of the molecules and peak intensity I_0 of the IR laser pulse. The velocity distribution data of the dispersed CS_2 molecules are shown in Fig. 6 and 7 for P_0 = 81 and 21 bar, respectively, for eight I_0 values. The peak intensities to form the optical standing wave are set as I_0 = 0.0, 0.8 × 10^10, 1.68 × 10^10, 2.48 × 10^10, 3.28 × 10^10, 3.98 × 10^10, 4.78 × 10^10 and 6.3 × 10^10 W/cm^2 from (a) to (h) in Fig. 6 and 7. In each data set, the top and middle image show the measured and simulated velocity distribution image, respectively. The accumulation time of every measured image is 1,200 seconds, which correspond to 12,000 laser shots. In the bottom of each data set, a measured velocity profile along the x-axis and corresponding simulation are plotted with a gray-filled curve and a black solid curve, respectively. Here, the velocity profiles are normalized so that they sum to 1.

For Fig. 6(a) and 7(a), in the absence of the laser field, their velocity distribution is dominated by the blue effect as we discussed previously. Thus, these two velocity profiles have the same velocity distribution. Within the standing wave field, the dispersion of the CS_2 molecules varies drastically with increasing the intensity I_0. The drifting maximum peak near the center of the x-axis and appearance of the outer peaks are the most noticeable difference. The drifting maximum peak near the center is due to the rotation in the phase space of the standing wave potential. The appearing outer peaks are associated with a rainbow-like singularity [9,61] These variances are much apparent in Fig. 6 (P_0 = 81 bar) because the state-dependent alignment effect appears clearly at the low rotational temperature T_{rot} = 1 K.

The simulations are performed to reproduce the molecular dispersion by the standing wave with considering the rotational state-dependent alignment effect. Here, we chose the $\langle v_{0x} \rangle$ value as 10 m/s based on comparing the width and center of velocity profiles between the simulations and the measurements. The difference of the velocity width ΔW and the velocity center ΔC at 50% ($W_{0.5}$ and $C_{0.5}$) and 10% ($W_{0.1}$ and $C_{0.1}$) of the maximum intensity show how well the simulations agree with the measurement at T_{rot} = 1 and 35 K in Fig. 8 and Fig. 9, respectively. The Fig. 8(a) shows $\Sigma_{I_0}(\Delta W)^2$, which indicates the sum of $(\Delta W)^2$ each of $W_{0.5}$ (blue), and $W_{0.1}$ (green), for the measured I_0 against the most probable initial velocity on the x-axis $\langle v_{0x} \rangle$ from 6 to 14 m/s. Furthermore, the variation ratio of the total $(\Delta W)^2$ is obtained by dividing each total $(\Delta W)^2$ at given initial velocity to the average of total $(\Delta W)^2$, which is termed $\langle \Sigma_{I_0}(\Delta W)^2 \rangle$, in Fig. 8(b). The comparison for the velocity centers is plotted at the Fig. 8(c) and (d) for the sum of $(\Delta W)^2$ and the variation ratio of the total $(\Delta C)^2$. The same analysis is performed for T_{rot} = 35 K at the Fig. 9. Here, the analysis of the velocity width and center show the minimized difference at $\langle v_{0x} \rangle$ = 10 m/s, except the velocity center at T_{rot} = 1 K. The velocity center

shows the minimal difference at $<v_{0x}> = 11$ and 12 m/s for of $W_{0.1}$ and $W_{0.5}$, respectively. Consequently, the dispersion simulations results agree with the measurements at $<v_{0x}> = 10$ m/s generally.

Additionally, the simulations using the alignment-considered polarizability $\alpha_{J,M}(I)$ and alignment-ignored polarizability $\alpha_{J,M}(0)$ are compared with the experimental data. Here, the effective polarizability $\alpha_{J,M}$ indicates $\alpha^U_{J,M}$. Figure 10 shows the comparison of the velocity widths with considering and ignoring alignment effect. The velocity profiles widths $W_{0.5}$ and $W_{0.1}$ about Fig. 6(e), where $I_0 = 3.2 \times 10^{10}$ W/cm^2, are indicated in Fig. 10(a). The profiles for the alignment-considered and alignment-ignored velocity are represented as black solid and dashed lines, respectively. For a more quantitative comparison of alignment-considered and alignment-ignored polarizabilities, the velocity widths of $W_{0.5}$ and $W_{0.1}$ at various laser intensities are compared with the experimental results in Fig. 10(b) for $T_{rot} = 1$ K and (c) for $T_{rot} = 35$ K. In the figures, the experimental data are plotted using blue triangles and green squares for $W_{0.5}$ and $W_{0.1}$, respectively. The calculations, which are performed with 100,000 molecules for precision, with and without considering alignment effect are represented with solid lines and dashed lines, respectively. The color code for the velocity width is shared with each other. As shown in Fig. 10(a), it is shown that the calculation with alignment-ignored polarizabilities can't reproduce the experimental data while the calculation with alignment-considered polarizabilities can reproduce more similarly. On the other hand, Fig. 10(c) shows almost the same velocity widths, except the wide tails, for any laser intensities due to the high rotational temperature. In Fig. 10(b), the abrupt changes of $W_{0.5}$ are obtained at different threshold laser intensities I_0^*. When I_0 is equal to I_0^*, the half period of the motion in phase space is similar to the duration of the pulsed standing wave τ, [14,62]. Here, the half period is proportional to the potential well depth, which is the product of $4I_0$ and $\alpha_{J,M}(4I_0)$ or $\alpha_{J,M}(0)$. Therefore, I_0^* is smaller for the molecule occupying rotational states of larger $\alpha_{J,M}(4I_0)$. Consequently, the different I_0^* values for the two simulations conditions make the different aspect of the velocity profiles in Fig. 10(a). The widening of $W_{0.1}$ with I_0 indicates that the potential well depth increases as a function of the laser field intensity I_0 and $\alpha_{J,M}(4I_0)$ or $\alpha_{J,M}(0)$ proportionally. Here, $W_{0.1}$ with considering alignment effect shows larger generally than the $W_{0.1}$ without considering alignment because $\alpha_{J,M}(4I_0)$ is larger than $\alpha_{J,M}(0)$ generally.

Consequently, the simulations with considering of alignment effect reproduce the experimental data much similarly. However, the simulation condition should be adjusted further for the correct reproduction of the experimental data. The simulation results with the alignment-ignored polarizability $\alpha_{J,M}(0)$ show strong disagreement with the experimental data for $T_{rot} = 1$ K. At the respectively high rotational temperature, $T_{rot} = 35$ K, the rotational state-dependent alignment effect is diluted thus the simulation with $\alpha_{J,M}(4I_0)$ and $\alpha_{J,M}(0)$ doesn't exhibit much different dispersion aspect. These comparisons show the effect of state-dependent molecular alignment on molecular scattering by an optical standing wave.
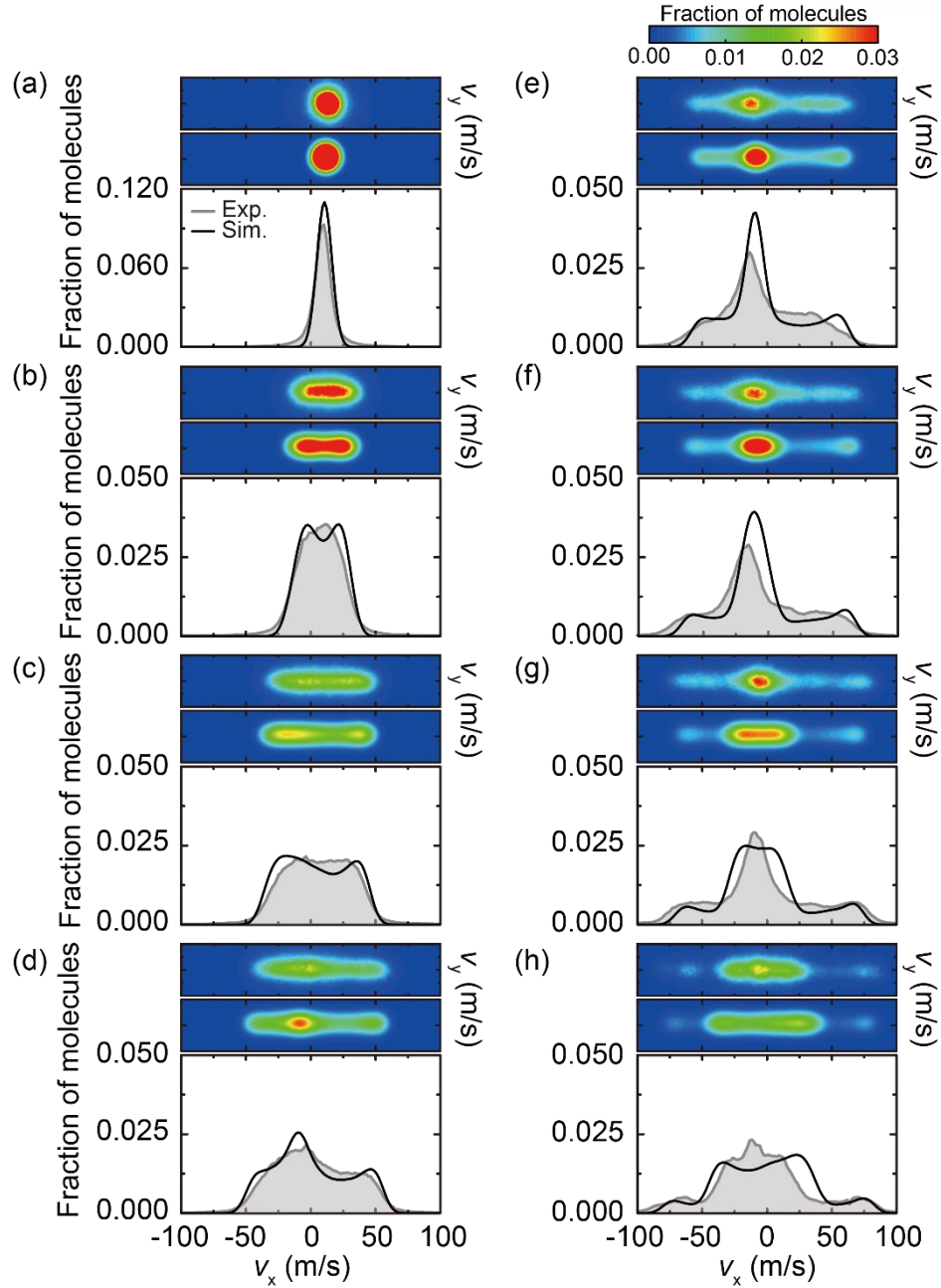
Figure 6. Dispersion of CS_2 molecules at $P_0 = 81$ bar with various intensities. Each set show the comparison of dispersion of CS_2 molecules with the calculations for different laser intensity $I_0 =$ (a) 0.0 (b) 0.8×10^{10} W/cm^2 (c) 1.6×10^{10} W/cm^2 (d) 2.4 $\times 10^{10}$ W/cm^2 (e) 3.2×10^{10} W/cm^2 (f) 3.9×10^{10} W/cm^2 (g) 4.7×10^{10} W/cm^2 (h) 6.3×10^{10} W/cm^2. Each set consists of the measured (first panel), simulated (second panel) velocity distribution along the x-axis at $P_0 = 81$ bar and their velocity profiles (third panel). To obtain the molecular dispersion, the accumulation time for every measurement is 1,200 seconds, which correspond to 12,000 laser shots. In the absence of the laser field, the velocity distribution is dominated by the detector blur effect. A increasing the laser field intensity, the velocity profiles show distinct change. The drifting peak and appearing outer peaks are noticeable. The simulations are agreed well with considering state-dependent alignment effect for $T_{rot} = 1$ K.

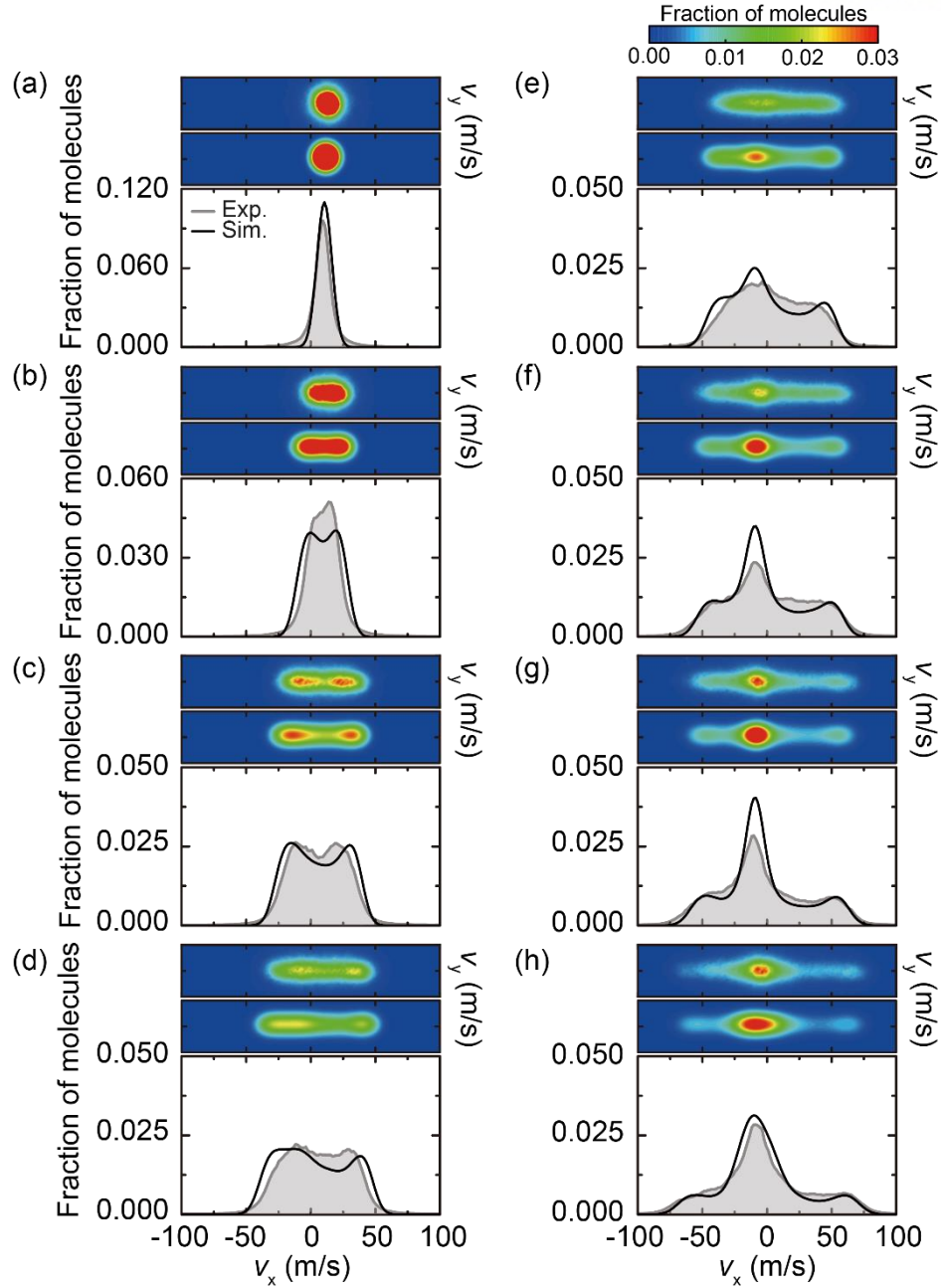**Figure 7.** Dispersion of CS_2 molecules at $P_0 = 21$ bar with various intensities. The measured (first panel) and simulated (second panel) velocity distribution along the x-axis at $P_0 = 21$ bar with their velocity profiles (third panel). For each data form (a) to (h), the laser intensity I_0 is equal with the corresponding data of Fig. 6. The accumulation time for every measurement is 1,200 seconds too. For $P_0 = 21$ bar, we estimate the rotational temperature as 35 K. Here, the dispersion aspect is not apparent as in $P_0 = 81$ bar data.
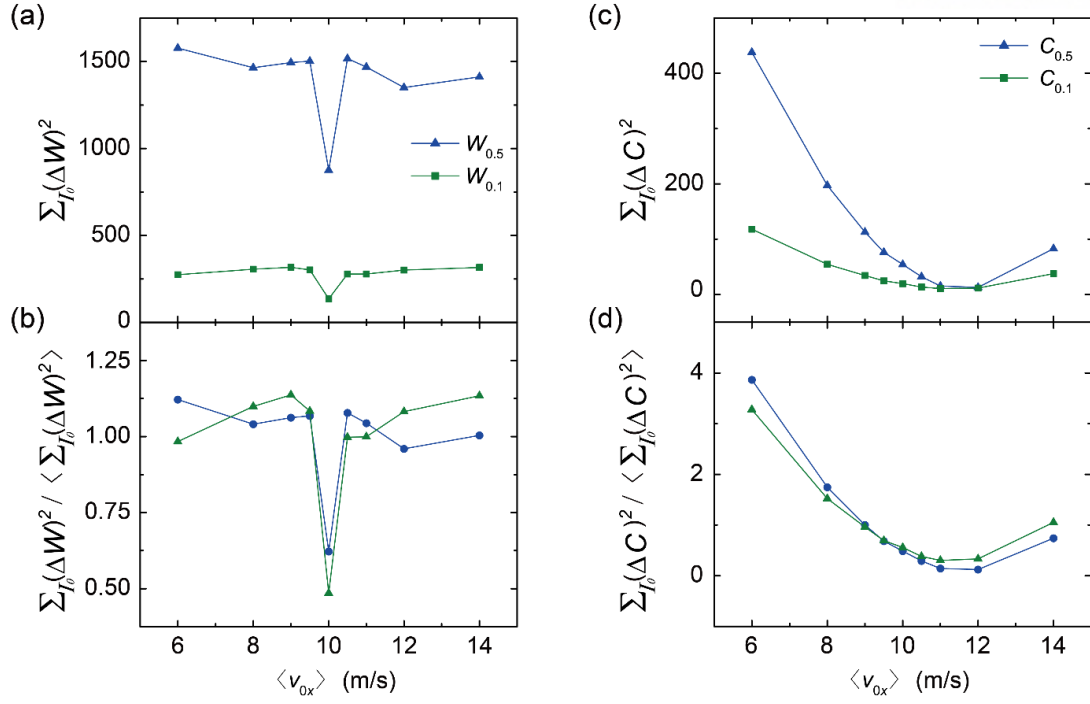
Figure 8. Difference of the velocity width ΔW and the velocity center ΔC about $W_{0.5}$ and $W_{0.1}$ at $T_{rot} = 1$ K. (a) The sum of $(\Delta W)^2$ about $W_{0.5}$ (blue) and $W_{0.1}$ (green) are plotted for the demonstrated I_0 against the most probable initial velocity on the *x*-axis $\langle v_{0x} \rangle$ from 6 to 14 m/s. (b) The variation ratio of the total $(\Delta W)^2$ is obtained by dividing each total $(\Delta W)^2$ at given initial velocity to the average of total $(\Delta W)^2$. The sum of $(\Delta C)^2$ and variation ratio of the total $(\Delta C)^2$ about $C_{0.5}$ (blue) and $C_{0.1}$ (green) are illustrated in (c) and (d), respectively. The velocity widths of the simulations agree with the measurement generally at $\langle v_{0x} \rangle$ = 10 m/s. The velocity center, however, shows the minimal difference at $\langle v_{0x} \rangle$ = 11 and 12 m/s for of $W_{0.1}$ and $W_{0.5}$, respectively.
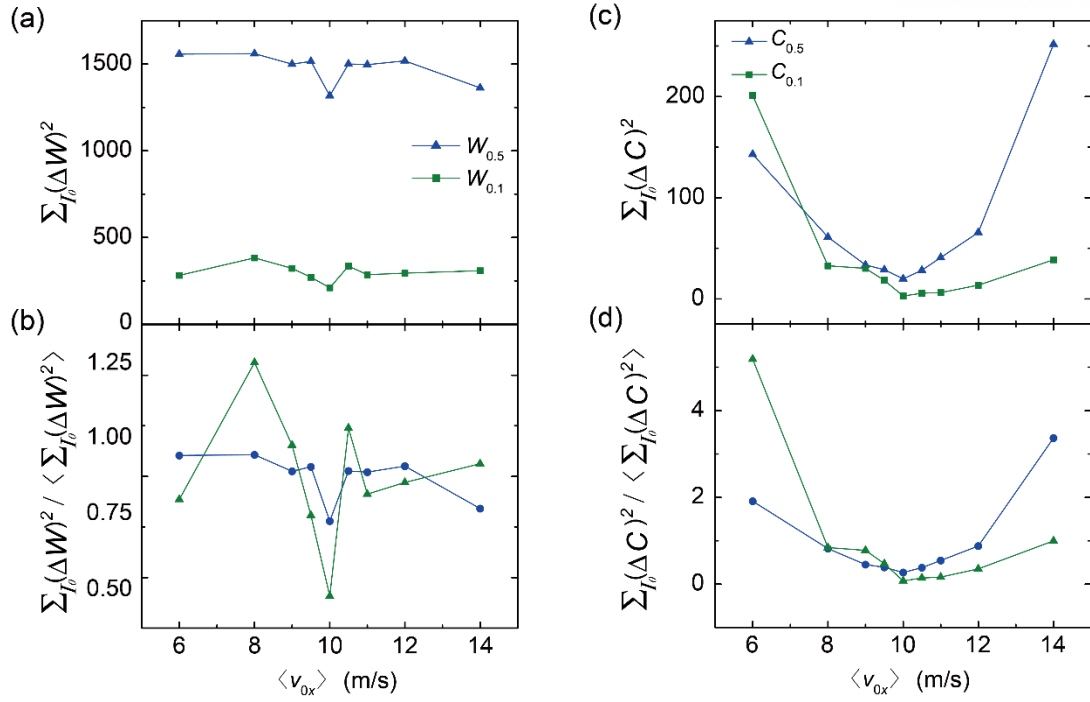
Figure 9. Difference of the velocity width ΔW and the velocity center ΔC about $W_{0.5}$ and $W_{0.1}$ at $T_{\text{rot}} = 35$ K. (a) The sum of $(\Delta W)^2$ each of $W_{0.5}$ (blue), and $W_{0.1}$ (green) for the demonstrated I_0 against $<v_{0x}>$ from 6 to 14 m/s. (b) The variation ratio of the total $(\Delta W)^2$ is obtained by dividing each total $(\Delta W)^2$ to $\langle \Sigma_{I_0}(\Delta W)^2 \rangle$ at given initial velocity. (c) The sum of $(\Delta C)^2$ and (d) variation ratio of the total $(\Delta C)^2$ are figured. The measured velocity widths and centers agree well with the simulations at $<v_{0x}>$ = 10 m/s. Consequently, we chose initial velocity along the x-axis of 10 m/s.
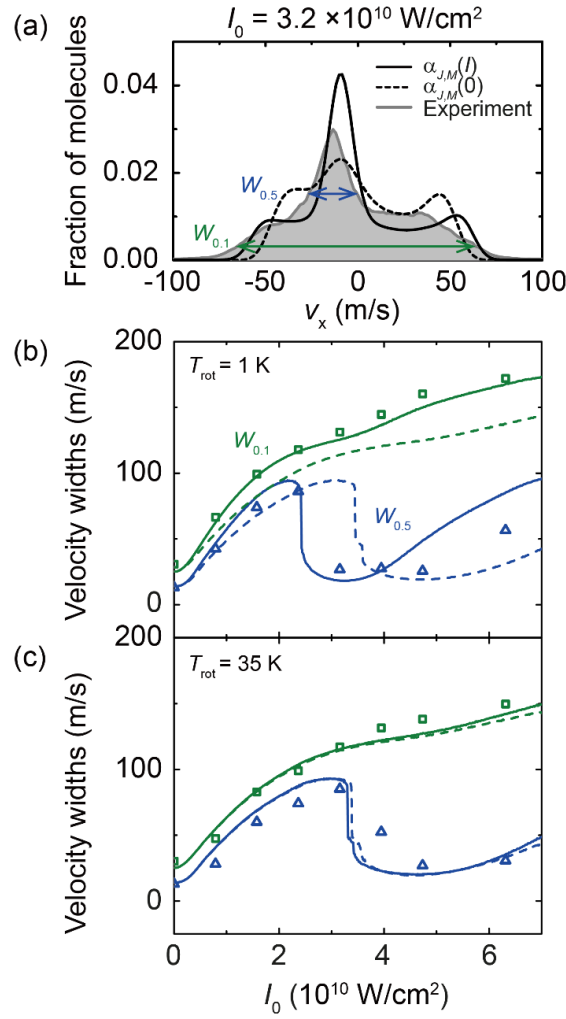
Figure 10. Comparison of the velocity profiles width. (a) The measured velocity profile and the simulation results with $\alpha_{J,M}(I)$ and $\alpha_{J,M}(0)$ for $I_0 = 3.2 \times 10^{10}$ W/cm^2 are plotted. The velocity profile for the measured data is represented using a gray-filled curve. The simulation result with (without) considering alignment effect is plotted using a black solid (dashed) line. The widths of the velocity profile at 50% (blue) and 10% (green) of the maximum intensity are indicated as $W_{0.5}$ and $W_{0.1}$, respectively. (b) The velocity width of $W_{0.5}$ and $W_{0.1}$ for the measured data at $P_0 = 81$ bar and simulated data with $\alpha_{J,M}(I)$ and $\alpha_{J,M}(0)$ at T_{rot} = 1 K are plotted as a function of the laser peak intensity. The simulation with $\alpha_{J,M}(I)$ reproduce well the dispersion aspect of measurement. (c) The same analysis was performed for the measurement at $P_0 = 21$ bar and for the simulation at $T_{\text{rot}} = 35$ K. Due to the high rotational temperature, the both simulation results show almost same aspect with well-agreement measured velocity profiles.

5. Conclusion

As a conclusion, we have shown how state-dependent alignment affects the optical dipole force in CS_2 molecules. Herein, we demonstrate the dispersion of carbon disulfide molecules using an optical standing wave at a stagnation pressure of 81 and 21 bar, which corresponds to T_{rot} = 1 and 35 K, respectively. The simulations of dispersion trajectories were performed to interpret the dispersion of the molecules with and without considering state-dependent alignment effect. At T_{rot} = 1 K, the state-dependent alignment effect becomes manifest due to the low-lying rotational states. Thus, the simulations that consider the state-dependent alignment effect reproduce the experimental data while the simulations that ignore the alignment effect on the polarizability exhibit strong disagreement. At T_{rot} = 1 K, a relatively high rotational temperature, the effect of the molecular alignment becomes weak because the molecules are in high-J rotational states, predominantly. Thus, the state-dependent alignment effect is smeared out. Thereby, the simulation with and without considering state-dependent alignment effect shows almost the same aspect of molecular dispersion. These results verify that the state-dependent alignment contributes the optical dipole force and is modeled correctly. Consequently, we propose the importance of considering the molecular alignment with their rotational states to manipulate molecules. By considering state-dependent alignment effect, we can interpret the optical dipole force more accurately. Furthermore, this study can provide a cornerstone to develop the molecular physics and new method, such as a selection of specific state of nonpolar molecules.

Appendix A.

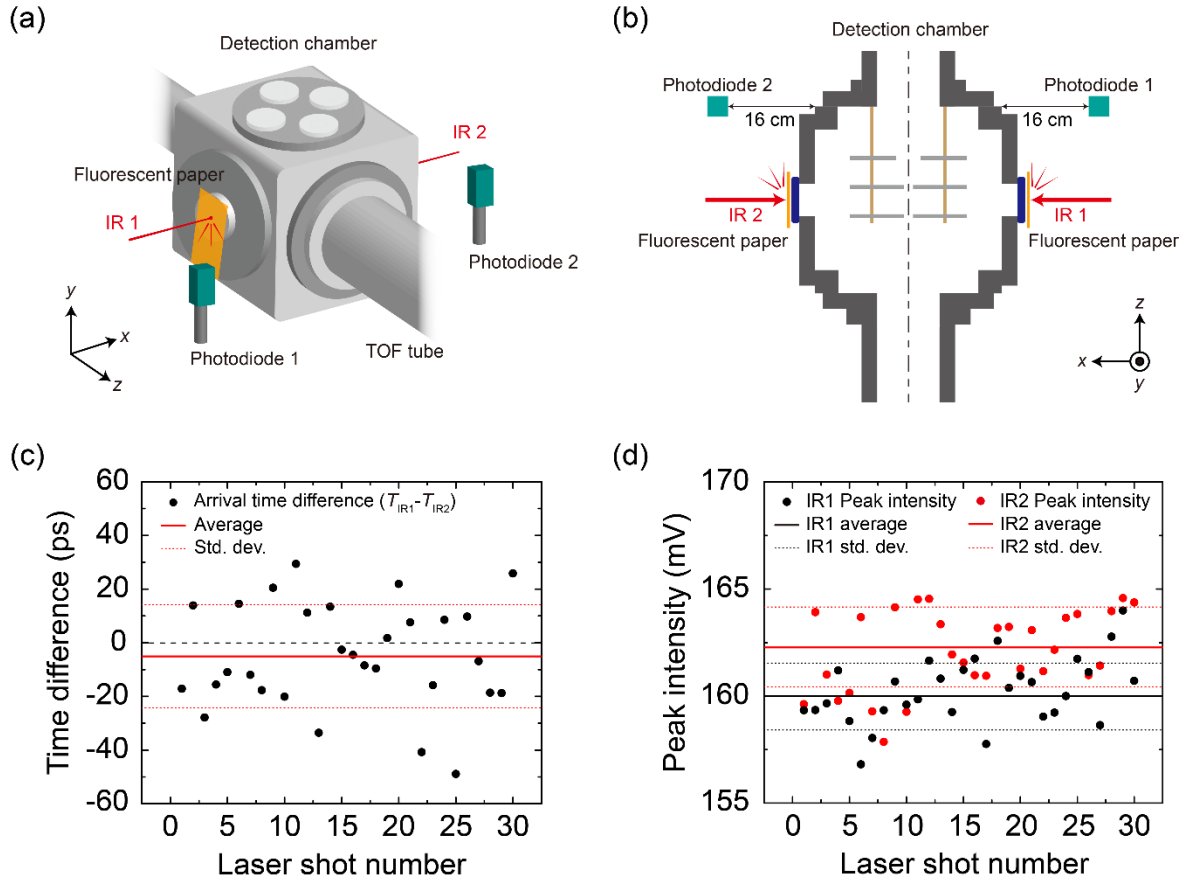# IR pulse analysis

(a)

(b)

(c)

(d)

Figure A. (a) 3-dimensional illustration for measuring the laser properties. (b) Top view of measuring scheme for the laser properties. (c) Arrival time difference between IR1 and IR2. (d) Peak intensity difference of IR1 and IR2 for each laser shot.

Two PIN photodiodes, known as a positive-intrinsic-negative diode, (EOT ET-2030) are used to measure the arrival times of the counter-propagating IR pulses, namely T_{IR1} and T_{IR2}. Each photodiode is located 16 cm apart from the corner of the detection chamber near the TOF tube symmetrically with respect to the z-axis. In a similar way, there are two fluorescent papers in front of the windows on both sides to make the IR pulses scattered. The photodiodes record the temporal profiles of each scattered pulse of IR1 and IR2 simultaneously. The 3-dimensional and 2-dimensional illustrations of measuring schemes are shown in Fig. A(a) and (b), respectively.

We recorded 30 temporal profiles each for the IR1 and IR2 with the pulse energy of 4 mJ, and then analyzed them to get their arrival times and power stability using a Gaussian function. The arrival time of pulses is obtained as the centers of the fitted curves. Each of the black points in Fig. A(c) show the

differences of arrival time between the IR1 and IR2 pulses. A red solid line and red dotted lines indicate the average value of arrival time difference (5.1 ps) and their standard deviation (19.7 ps), respectively. Because the pulse duration of the IR beam (7.5 ns) is much longer than the arrival time difference, the arrival time difference is so trivial that it can be ignored.

The recorded peak intensities of pulses are plotted in Fig. A(d) as black (red) dots for the IR1 (IR2) pulses. I plotted here also lines for an average value (standard deviation) using a solid (dotted) lines. The average of peak intensities (standard deviation) are estimated as 160.0 mV (1.59 mV) and 162.4 mV (1.94 mV) for IR1 and IR2, and therefore the power stabilities of IR1 and IR2 pulses were estimated as 0.994% and 1.195%, respectively.

Appendix B

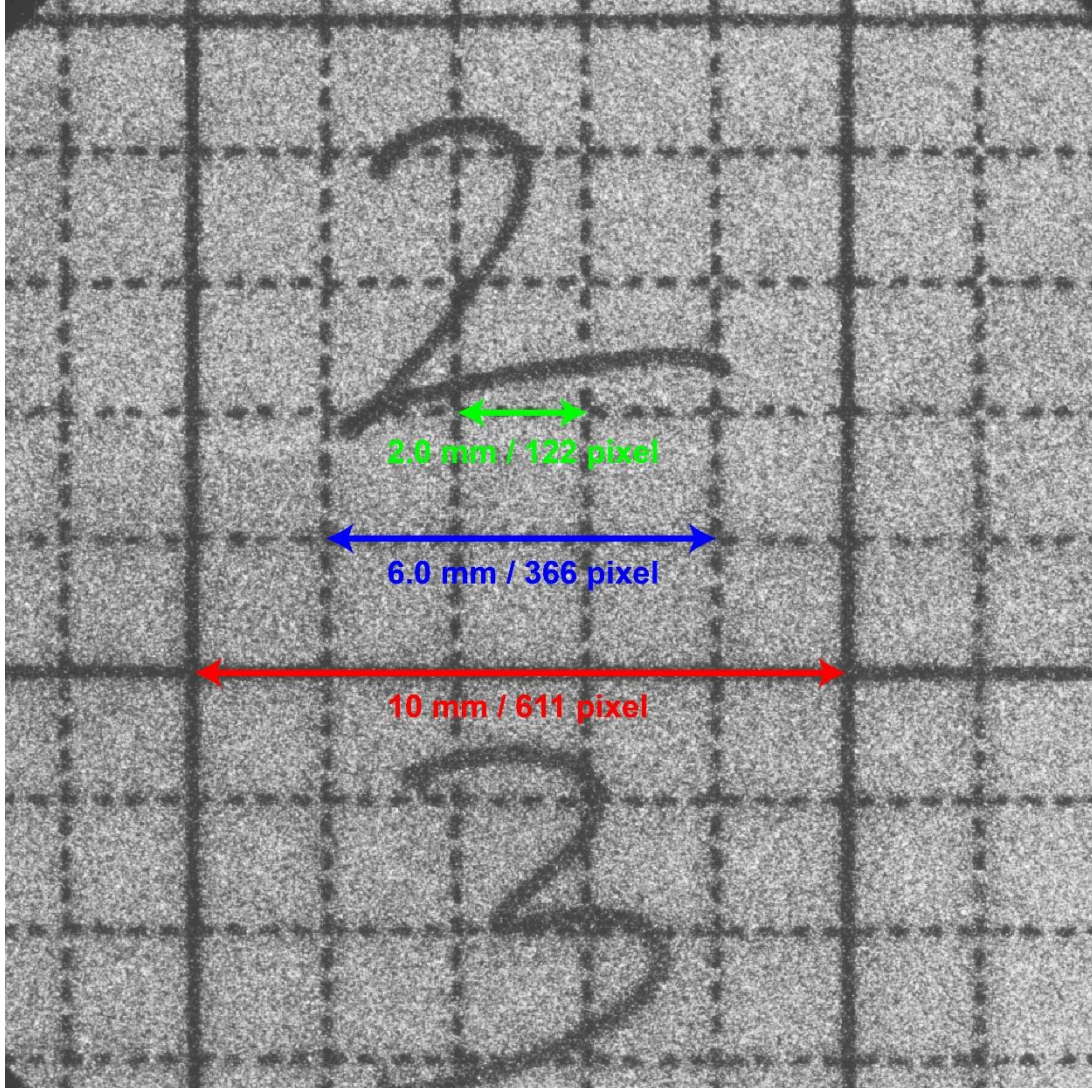# Calibrating pixel resolution of the ICCD camera

Figure B. Obtained image of a graph paper using ICCD camera.

Figure B shows a graph paper captured by the ICCD camera to calibrate the pixel resolution of the ICCD camera. We installed a macro lens of AF-S Micro NIKKOR 60 mm f/2.8G ED (Nikon's equivalent of a macro lens) on the ICCD camera and stuck the graph paper, which has an interval of 10 mm of solid lines, on the rear surface of the phosphor screen. As a result of calibration, the pixel resolution of the ICCD camera is 16.4 μm/pixel.

Appendix C

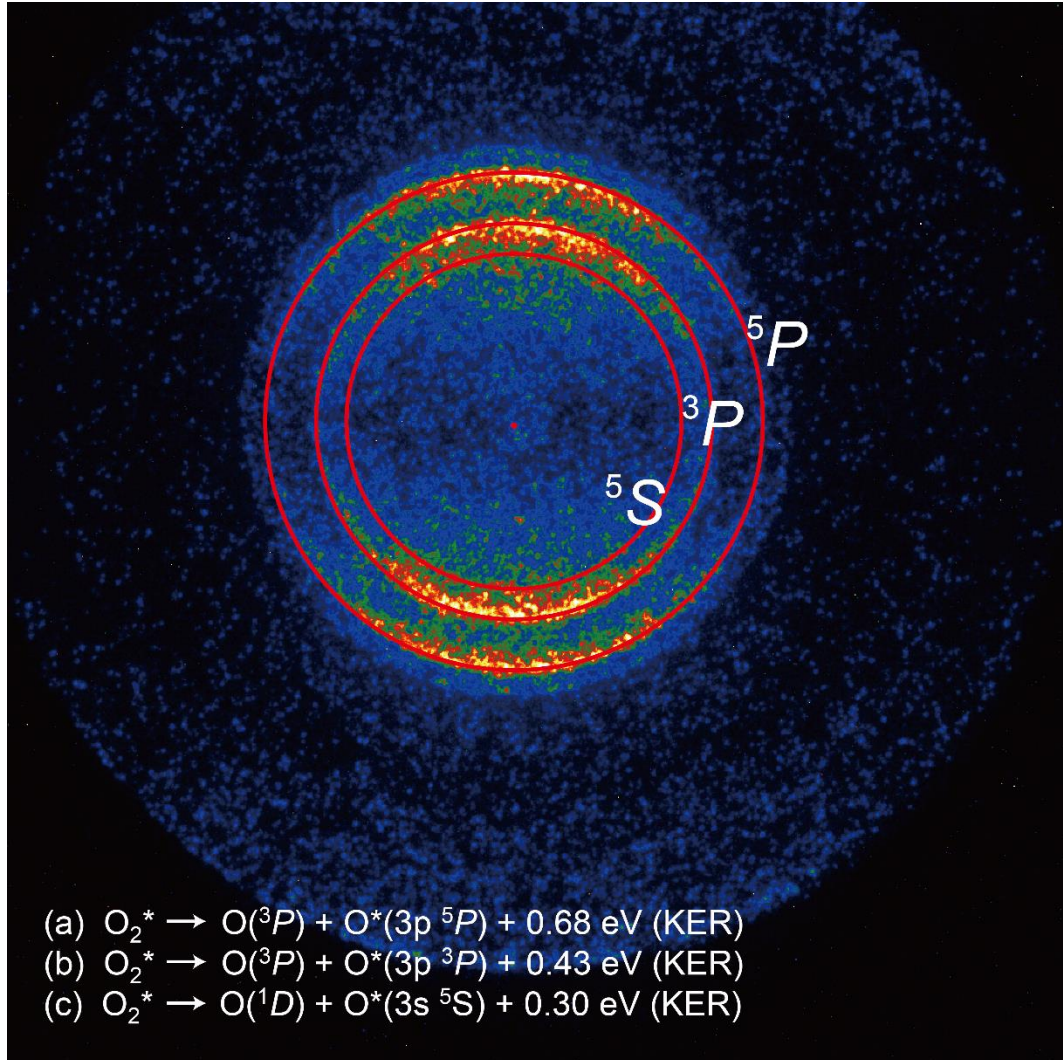# Magnification factor of velocity map imaging

Figure C.1. Velocity map image of oxygen fragments.

To calibrate the magnification factor of the velocity map imaging of our experimental system, fragmentation of oxygen molecules is used as a reference because this reaction has been studied well [60]. The calibration is performed by the comparison between measured and calculated velocities. The O_2 molecule absorbs the third photon after two-photon excitation to the Rydberg state to form a superexcited state $O_2{}^*$ which decays in several channels as shown below:

(a) $O_2{}^* \rightarrow O(^3P) + O^*(3p\ ^5P) + 0.68$ eV (KER)
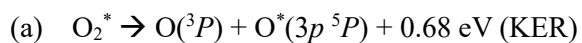
(b) $O_2^* \rightarrow O(^3P) + O^*(3p\ ^3P) + 0.43$ eV (KER)

(c) $O_2^* \rightarrow O(^1D) + O^*(3s\ ^5S) + 0.30$ eV (KER)

Here, the total kinetic energy release (KER) must be divided between two fragmented O atoms.

　　Figure C.1 shows the velocity map image of oxygen fragmentations at 224.96 nm with the red circles indicating the calculated contour lines for a speed of each fragment. The speed of the fragmented two oxygen atoms can be calculated using the equation for the kinetic energy release (KER) of via:

$$\frac{1}{2}m_O v^2 \times 2 = E_{KER}, \tag{12}$$

where m_O is the mass of an oxygen atom. Thus, the speeds of a fragmented oxygen atom are calculated for each process by the below equations, respectively.

$$v = \sqrt{\frac{E_{KER}}{m_O}} = \sqrt{\frac{0.68 \times e}{15.999 \times 10^{-3} \div N_A}} = 2025.1 \text{ m/s}, \tag{13a}$$

$$v = \sqrt{\frac{E_{KER}}{m_O}} = \sqrt{\frac{0.43 \times e}{15.999 \times 10^{-3} \div N_A}} = 1610.3 \text{ m/s}, \tag{13b}$$

$$v = \sqrt{\frac{E_{KER}}{m_O}} = \sqrt{\frac{0.30 \times e}{15.999 \times 10^{-3} \div N_A}} = 1345.1 \text{ m/s}, \tag{13c}$$

Here, N_A and e are Avogadro's number and elementary charge, respectively.
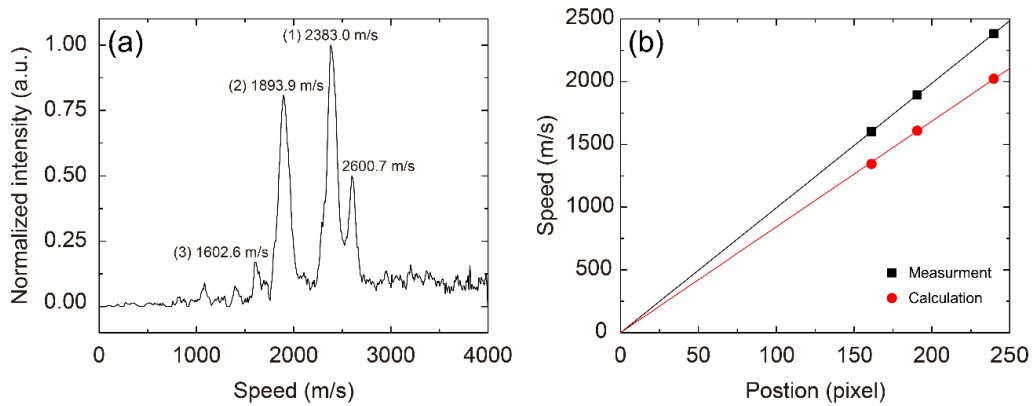

Figure C.2. (a) Speed distribution of the obtained fragment image. (b) Comparison of the obtained speed and the calculated

for each fragmentation channel.

The captured image is analyzed with the speed distribution after reconstruction via an Abel inversion using the Basis-Set Expansion method (BASEX) [63]. The speed distribution of the obtained image is presented in Fig. C.2(a) with labels of three fragmentation processes. The outermost peak at 2600.7 m/s, corresponding to total KER of 0.81 eV, is undefined. Figure C.2(b) shows the measured (black squares) and calculated (red circles) speed for each fragmentation process. The magnification of velocity map imaging can be calibrated by the ratio between the measured and calculated speed of each fragmentation process. The slope of measured speeds for their positions is 9.94 m/s·pixel while the slope of calculated speeds is 8.43 m/s·pixel. Here, the intercepts of the linearly fitted lines must be fixed at the zero because the speed of a fragmented atom must be zero at the zero position. Thus, the magnification factor of velocity map imaging is obtained as 1.18. In other words, the obtained image must be corrected 1.18 times smaller because the detector obtains 1.18 times magnified image than the ideal image in our experimental system.

References

[1] A. Ashkin, "Acceleration and trapping of particles by radiation pressure", Phys. Rev. Lett. **24**, 156 (1970).

[2] J. E. Bjorkholm, R. R. Freeman, A. Ashkin, and D. B. Pearson, "Observation of Focusing of Neutral Atoms by the Dipole Forces of Resonance-Radiation Pressure", Phys. Rev. Lett. **41**, 1361 (1978).

[3] E. M. Rasel, M. K. Oberthaler, H. Batelanan, J. Schmiedmayer, and A. Zeilinger, "Atom Wave Interferometry with Diffraction Gratings of Light", Phys. Rev. Lett. **75**, 2633 (1995).

[4] B. Segev, R. Cote, and M. G. Raizen, "Quantum reflection from an atomic mirror", Phys. Rev. A **56**, R3350 (1997).

[5] H. Stapelfeldt, H. Sakai, E. Constant, and P. B. Corkum, "Deflection of Neutral Molecules using the Nonresonant Dipole Force", Phys. Rev. Lett. **79**, 2787 (1997).

[6] B. S. Zhao, H. S. Chung, K. Cho, S. H. Lee, S. Hwang, J. Yu, Y. H. Ahn, J. Y. Sohn, D. S. Kim, W. K. Kang, and D. S. Chung, "Molecular Lens of the Nonresonant Dipole Force", Phys. Rev. Lett. **85**, 2705 (2000).

[7] H. S. Chung, B. S. Zhao, S. H. Lee, S. Hwang, K. Cho, S.-H. Shim, S.-M. Lim, W. K. Kang, and D. S. Chung, "Molecular lens applied to benzene and carbon disulfide molecular beams", J. Chem. Phys. **114**, 8293 (2001).

[8] B. S. Zhao, S. H. Lee, H. S. Chung, S. Hwang, W. K. Kang, B. Friedrich, and D. S. Chung, "Separation of a benzene and nitric oxide mixture by a molecule prism", J. Chem. Phys. **119**, 8905 (2003).

[9] X. N. Sun, L. Y. Kim, B. S. Zhao, and D. S. Chung, "Rotational-State-Dependent Dispersion of Molecules by Pulsed Optical Standing Waves", Phys. Rev. Lett. **115**, 223001 (2015).

[10] X. N. Sun, B. G. Jin, L. Y. Kim, B. J. Kim, and B. S. Zhao, "Strong Optical Dipole Force Exerted on Molecules Having Low Rotational Temperature", ChemPhyChem **17**, 3701 (2016).

[11] R. Fulton, A. I. Bishop, and P. F. Barker, "Optical Stark Decelerator for Molecules", Phys. Rev. Lett. **93**, 243004 (2004).

[12] S. M. Purcell, and P. F. Barker, "Controlling the optical dipole force for molecules with field-induced alignment", Phys. Rev. A **82**, 033433 (2010).

[13] J. Ramirez-Serrano, K. E. Strecker, and D. W. Chandler, "Modification of the velocity distribution of H_2 molecules in a supersonic beam by intense pulsed optical gradients", Phys. Chem. Chem. Phys. **8**, 2985 (2006).

[14] R. Fulton, A. I. Bishop, M. N. Shneider, and P. F. Barker, "Controlling the motion of cold molecules with deep periodic optical potentials", Nat. Phys. **2**, 465 (2006).

[15] A. I. Bishop, L.Wang, and P. F. Barker, "Creating cold stationary molecular gases by optical Stark deceleration", New J. Phys. **12**, 073028 (2010).

[16] S. Chu, "The manipulation of neutral particles", Rev. Mod. Phys. **70**, 685 (1998).

[17] C.N. Cohen-Tannoudji, "Manipulating atoms with photons", Rev. Mod. Phys. **70**, 707 (1998).

[18] W.D. Phillips, "Laser cooling and trapping of neutral atoms", Rev. Mod. Phys. **70**, 721 (1998).

[19] M.H. Anderson, J.R. Ensher, M.R. Matthews, C.E. Wieman, and E.A. Cornell, "Observation of Bose-Einstein Condensation in a Dilute Atomic Vapor", Science **269**, 198 (1995).

[20] K.B. Davis, M.O. Miewes, M.R. Andrews, N.J. van Druten, D.S. Durfee, D.M. Kurn, and W. Ketterle, "Bose-Einstein condensation in a gas of sodium atoms", Phys. Rev. Lett. **75**, 3969 (1995).

[21] E.A. Cornell, and C.E. Wieman, "Bose-Einstein condensation in a dilute gas, the first 70 years and some recent experiments", Rev. Mod. Phys. **74**, 875 (2002).

[22] W. Ketterle, "When atoms behave as waves: Bose-Einstein condensation and the atom laser", Rev. Mod. Phys. **74**, 1131 (2002).

[23] S. Chu, "Laser Manipulation of Atoms and Particles", Science **253**, 861 (1991).

[24] T. T. Perkins, S. R. Quake, D. E. Smith, and S. Chu, "Relaxation of a single DNA molecule observed by optical microscopy", Science **264**, 822 (1994).

[25] A. Ashkin, K. Schütze, J. M. Dziedzic, U. Euteneuer, and M. Schliwa, "Force generation of organelle transport measured in vivo by an infrared laser trap", Nature **348**, 346 (1990).

[26] J. T. Finer, R.M. Simmons, and J. A. Spudich, "Single myosin molecule mechanics: piconewton forces and nanometre steps", Nature **368**, 113 (1994).

[27] A. Ashkin, and J. M. Dziedzic, "Optical trapping and manipulation of viruses and bacteria", Science **235**, 1517 (1987).

[28] A. Ashkin, J. M. Dziedzic and T. Yamane, "Optical trapping and manipulation of single cells using infrared laser beams", Nature **330**, 769 (1987).

[29] A Jonáš, and P. Zemanek, "The use of optical forces for particle manipulation, sorting, and analysis", Electrophoresis **29**, 4813 (2008).

[30] C. S. Adams, and E. Riis, "Laser cooling and trapping of neutral atoms", Prog. Quant. Electron. **21**, 1 (1997).

[31] B. J. Sussman, J. G. Underwood, R. Lausten, M. Y. Ivanov, and A. Stolow, "Quantum control via the dynamic Stark effect: Application to switched rotational wave packets and molecular axis alignment", Phys. Rev. A **73**, 053403 (2006).

[32] R. Fulton, A. I. Bishop, P. F. Barker, "Focusing ground-state xenon in a pulsed optical field", Phys. Rev. A **71**, 043404 (2005).

[33] E. S. Shuman, J. F. Barry, D. R. Glenn, and D. DeMille, "Radiative Force from Optical Cycling on a Diatomic Molecule", Phys. Rev. Lett. **103**, 223001 (2009).

[34] J. F. Barry, E. S. Shuman, E. B. Norrgard, and D. DeMille, "Laser radiation pressure slowing of a molecular beam", Phys. Rev. Lett. **108**, 103002 (2012).

[35] J. F. Barry, D. McCarron, E. B. Norrgard, M. Steinecker, and D. DeMille, "Magneto-optical trapping of a diatomic molecule", Nature. **512**, 286 (2014).

[36] M. Yeo, M. T. Hummon, A. L. Collopy, B. Yan, B. Hemmerling, E. Chae, M. Doyle, and J. Ye, "Rotational state microwave mixing for laser cooling of complex diatomic molecules", Phys. Rev. Lett. **114**, 223003 (2015).

[37] B. Friedrich and D. Herschbach, "Alignment and Trapping of Molecules in Intense Laser Fields", Phys. Rev. Lett. **74**, 4623 (1995).

[38] T. Seideman, "Molecular optics in an intense laser field: A route to nanoscale material design", Phys. Rev. A **56**, 17 (1997).

[39] T. Seideman, "On the dynamics of rotationally broad, spatially aligned wave packets", J. Chem. Phys. **115**, 5965 (2001).

[40] B. Friedrich, "Slowing of supersonically cooled atoms and molecules by time-varying nonresonant induced dipole forces", Phys. Rev. A **61**, 025403 (2000).

[41] L. Y. Kim, J. H. Lee, H. A. Kim, S. K. Kwak, B. Friedrich, and B. S. Zhao, "Effect of rotational-state-dependent molecular alignment on the optical dipole force", Phys. Rev. A **94**, 013428 (2016).

[42] B. Friedrich, and D. Herschbach, "Spatial orientation of molecules in strong electric fields and evidence for pendular states", Nature **353**, 412 (1991).

[43] V. A. Cho, and R. B. Bernstein, "Tight focusing of beams of polar polyatomic molecules via the electrostatic hexapole lens", J. Phys. Chem. **95**, 8129 (1991).

[44] B. Friedrich, and D. Herschbach, "Polarization of molecules induced by intense nonresonant laser fields", J. Phys. Chem., **99**, 15686 (1995).

[45] J. Ortigoso, M. Rodr´ıguez, M. Gupta, and B. Friedrich, "Time evolution of pendular states created by the interaction of molecular polarizability with a pulsed nonresonant laser field", J. Chem. Phys. **110**, 3870 (1999).

[46] H. Sakai, C. P. Safvan, J. J. Larsen, K. M. Hilligsqe, K. Hald, and H. Stapelfeldt, "Controlling the alignment of neutral molecules by a strong laser field", J. Chem. Phys., **110**, 10235 (1999).

[47] J. J. Larsen, H. Sakai, C. P. Safvan, I. Wendt-Larsen, and H. Stapelfeldt, "Aligning molecules with intense nonresonant laser fields", J. Chem. Phys., **111**, 7774 (1999).

[48] B. Friedrich, and D. R. Herschbach, "Manipulating molecules via combined static and laser fields", J. Phys. Chem. A **103**, 10280 (1999).

[49] B. Friedrich, and D. R. Herschbach, "Enhanced orientation of polar molecules by combined electrostatic and nonresonant induced dipole forces", J. Chem. Phys. **111**, 6157 (1999).

[50] H. Sakai, S. Minemoto, H. Nanjo, H. Tanji, and T. Suzuki, "Controlling the orientation of polar molecules with combined electrostatic and pulsed, nonresonant laser fields", Phys. Rev. Lett. **90**, 083001 (2003).

[51] L. Holmegaard, J. H. Nielsen , I. Nevo, and H. Stapelfeldt, "Laser-induced alignment and orientation of quantum-state-selected large molecules", Phys. Rev. L **102**, 023001 (2009).

[52] H. Tanji, S. Minemoto, and H. Sakai, "Three-dimensional molecular orientation with combined electrostatic and elliptically polarized laser fields", Phys. Rev. A **72**, 063401 (2005).

[53] I. Nevo, L. Holmegaard, J. H. Nielsen, J. L. Hansen, H. Stapelfeldt, F. Filsinger , G. Meijer and J. Küpper, "Laser-induced 3D alignment and orientation of quantum state-selected molecules", Phys. Chem. Chem. Phys. **11**, 9912 (2009).

[54] R. Torres, R. de Nalda, and J. P. Marangos, "Dynamics of laser-induced molecular alignment in the impulsive and adiabatic regimes: A direct comparison", Phys. Rev. A **72**, 023420 (2005).

[55] M. Lemeshko, R. V. Krems, J. M. Doyle, and S. Kais, "Manipulation of molecules with electromagnetic fields", Mol. Phys. **111**, 1648 (2013).

[56] T. Seideman, "Shaping molecular beams with intense light", J. Chem. Phys. **107**, 10420 (1997).

[57] J. Baker, M. Konstantaki, and S. Couris, "A resonance enhanced multiphoton ionization study of the CS_2 molecule: The $4p$ Rydberg states", J. Chem. Phys. **103**, 2436 (1995).

[58] R. A. Morgan, M. A. Baldwin, A. J. Orr-Ewing, M. N. R. Ashfold, W. J. Buma, J. B. Milan, and C. A. de Lange, "Resonance enhanced multiphoton ionization spectroscopy of carbon disulphide", J. Chem. Phys. **104**, 6117 (1996).

[59] A. T. J. B. Eppink, and D. H. Parker, "Velocity map imaging of ions and electrons using electrostatic lenses: Application in photoelectron and photofragment ion imaging of molecular oxygen", Rev. Sci. Instrum. **68**, 3477 (1997).

[60] D. H. Parker, and A. T. J. B. Eppink, "Photoelectron and photofragment velocity map imaging of state-selected molecular oxygen dissociation/ionization dynamics", J. Chem. Phys. **107**, 2357 (1997).

[61] E. Gershnabel and I. S. Averbukh, "Deflection of field-free aligned molecules", Phys. Rev. Lett. **104**, 153001 (2010)

[62] G. Dong, W. Lu, and P. F. Barker, "Decelerating and bunching molecules with pulsed traveling optical lattices", Phys. Rev. A **69**, 013409 (2004).

[63] V. Dribinski, A. Ossadtchi, V. A. Mandelshtam, H. Reisler, "Reconstruction of Abel-transformable images: The Gaussian basis-set expansion Abel transform method", Rev. Sci. Instrum. **73**, 2634 (2002)

Acknowledgement

Frist of all, I would like to express my deep sense of gratitude to my advisor, Bum Suk Zhao who gave me the great opportunity to study this topic. I had a chance to get to know many things and I'm still leaning a lot from him. I also appreciate to professor Oh-Hoon Kwon and professor Thomas Schultz, sincerely. My dissertation could be completed thanks to their encouragement and guidance.

I am thankful to my colleagues Ju Hyun Lee, Tae Woo Kim and Bong Jun Kim. Especially, I want to say thank you from the bottom of my heart to Lee Young Kim and Xing Nan Sun. I got a great help from her in the simulations. Xing Nan Sun trained me to handle the lots of optics and lasers.

Lastly, I would like to thank all those who helped me in any way in my project.

Byung Gwun Jin